DE TTK

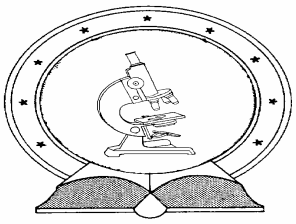

1949

Photon and electron induced transformations and pattern formation in amorphous chalcogenide nano-layers

Ph.D. Thesis
Egyetemi doktori (Ph.D.) értekezés

Viktor Takáts

Supervisor / Témavezető

Prof. Sándor Kökényesi

University of Debrecen
PhD School in Physics
Debreceni Egyetem
Természettudományi Doktori Tanács
Fizikai Tudományok Doktori Iskolája
Debrecen, 2012.

Ezen értekezést a Debreceni Egyetem Természettudományi Doktori Tanács *Fizikai tudományok* Doktori Iskola *Szilárdtestfizika és anyagtudomány* programja keretében készítettem a Debreceni Egyetem természettudományi doktori (PhD) fokozatának elnyerése céljából.

Debrecen, 2012.. . . . . .

Takáts Viktor

Tanúsítom, hogy *Takáts Viktor* doktorjelölt 2005 – 2009 között a fent megnevezett Doktori Iskola *Szilárdtestfizika és anyagtudomány* programjának keretében irányításommal végezte munkáját. Az értekezésben foglalt eredményekhez a jelölt önálló alkotó tevékenységével meghatározóan hozzájárult. Az értekezés elfogadását javasolom.

Debrecen, 2012 . . . . . .

Kökényesi Sándor
témavezető

Photon and electron induced transformations and pattern formation in amorphous chalcogenide nano-layers

Értekezés a doktori (Ph.D.) fokozat megszerzése érdekében
a fizika tudományágban

Írta: Takáts Viktor okleveles fizikus

Készült a Debreceni Egyetem Fizikai Tudományok doktori iskolája
(Szilárdtestfizika és anyagtudomány programja) keretében

Témavezető: Dr. Kökényesi Sándor

A doktori szigorlati bizottság:

elnök: Dr. .....
tagok: Dr. .....
Dr. .....

A doktori szigorlat időpontja: 2011…… … .

Az értekezés bírálói:

Dr. .....
Dr. .....

A bírálóbizottság:

elnök: Dr. .....
tagok: Dr. .....
Dr. .....
Dr. .....
Dr. .....

Az értekezés védésének időpontja: 2012 …… … .

Content

Preface

Amorphous chalcogenide materials are composites or alloys of VI-group elements (selenium, sulphur or tellurium) with other electropositive elements. These materials are in the front of the main interest of fundamental materials science, applied research and developments. Selenium itself is a well known material for modeling stimulated structural transformations and electron-hole processes in disordered solids, and has been used as a photosensitive semiconductor in different devices for almost one hundred years [1]. During the last few decades some complex chalcogenides based on As(Sb,Ge)-S(Se,Te) systems have been developed and investigated (see for example [2]). By changing the composition, a wide range of thermodynamical, mechanical, electrical and optical parameters can be achieved in these wide band gap semiconductors, which in turn determine applications in photonics, micro- and last time even in nanoelectronics [3].

Amorphous semiconductors belong to the class of disordered solids which exist in a non-equilibrium thermodynamical state. Accordingly, their flexible structures are readily affected by external influences, such as light, heat, e-beam or pressure, resulting in different metastable states and related changes of the above mentioned parameters. Such changes can be reversible or non-reversible, pointing from amorphous to amorphous state or from amorphous to crystalline one, depending on the composition, structure, technology or type of excitation.

The progress of materials science towards nanotechnology and nanostructures has affected chalcogenide research. CdS nanocrystals in a glass matrix were among the first nanocomposites used as optical filters and particularly chalcogenide glasses (ChG) were used in the re-writable optical discs and memory elements. Size constrictions in one-, two- or three dimensions can change the thermodynamical and mechanical parameters, as well as optical and electrical characteristics in spite of the more or less disordered structure of ChG [4].

Nanomultilayers (NML) made of crystalline materials by basic epitaxial technology [5] are among the best artificial nanocomposites, used widely as superlattices. On the other hand, NML produced from amorphous chalcogenides by different vacuum deposition techniques are in the stage of intensive investigation [6, 7].

Multilayers give a new, additional degree of freedom for tailoring the structure and physical properties. These include micro hardness, conductivity and optical parameters; however, new composites can also be created, which are difficult to produce by simpler synthesis methods.

Intermixing and interdiffusion processes are dedicated and even unique in tailoring the properties of NML, if one influences them through special treatments. Simple concentration gradients or further excitations can induce diffusion between the layers in NML. Investigations of induced interdiffusion in nano-multilayers are beneficial for fundamentals of materials science at nanoscale, and have potential applications in optical recording, fabrication of optical elements with spatial phase or amplitude modulation reliefs.

At present most of the photo-induced structural changes in amorphous chalcogenides are supposed to be related to electron-hole excitation, defect creation and atomic displacements, nevertheless the exact mechanism is still not properly understood. Induced changes in chalcogenide materials, thin layers or multilayers, caused by different excitations seem to have some common origin. However, it is a complex process which includes several effects, such as charge generation, defect creation and bond-switching, photo-induced plasticity, expansion or contraction, micro-hardness change and change of optical, electrical parameters, photo-oxidation and appearance of internal repulsive or attractive forces due to electrostatic interactions of charged defects.

The goal of our work was to clarify and separate processes which determine stimulated changes of volume and/or optical parameters in selected amorphous chalcogenide layers and nano-multilayers. The knowledge makes it possible for us to design and apply optical or geometrical reliefs produced by light or e-beams to elements of photonics [8].

1. Introduction

Glasses are, by definition, non-crystalline solids which are described as a separate discipline in solid state physics. Nowadays they are widely used in many industrial and laboratory applications. Glasses can be divided into several groups. Among the most common ones are oxide glasses (B_2O_3, SiO_2, GeO_2, P_2O_5), halides (BeF_2, $ZnCl_2$, ZrF_2), metallic glasses (compounds based on Au, Ag, Sb, Bi) and chalcogenide glasses (compounds based on S, Se, Te as As_2S_3, As_2Se_3, GeS).

In the 1950s, professors Goryunova and Kolomiets at the A.F. Ioffe Physico-Technical Institute in Leningrad found semiconductor behaviors of electrical conductivity in the ternary alloyed amorphous chalcogenides [9]. Chalcogenide glasses or, more generally amorphous chalcogenides are also known as excellent materials for optoelectronics. Their properties are easily tunable not only by technology but also by external excitations such as light, e-beam or other sources of energy. Many applications based on ChG have recently appeared on the market, such as DVD discs, solar cells or memory elements, monitors, etc. The new technology-based applications serve as a driving force for investigations of these materials, since their properties hide many prospective opportunities in different fields of electronics, as an active media of optical or optoelectronic devices.

The interest in amorphous materials is caused by the wide range of tunable properties and comparatively easy technological issues. Samples can be prepared by liquid phase processing and thermal vacuum evaporation, sputtering or deposition techniques onto different substrates. Key characteristics like electrical conductivity, refractive index and others often are quite unique and depend on the composition, fabrication technologies or sample preparation conditions. Thus, in the same material one can observe different and sometimes even opposite effects which can be reversible or non-reversible (crystallization/amorphyzation, light induced darkening/bleaching, volume changes, softening/hardening).

The transition of technology towards chalcogenide multilayers or nanolayered structures (NLS) with compositional modulations in the 3-20 nm range opened a new

chapter in the investigation of amorphous chalcogenides. When the modulation period of layers falls in the range of few nanometers, this technique opens new possibilities for tailoring the properties, and for the development of basic theories and applied solutions for photonics and electronics.

There exist numerous descriptions of mechanisms and models of metastability and structural transformations in amorphous chalcogenides; however, they are still not complete or are even contradictory. The present thesis contains new results and conclusions which have been drawn on the basis of my investigations of nanolayered chalcogenide structures as well as their separate components. The obtained results give us a new insight into the mechanisms of stimulated transformations and characteristics of the metastable solid amorphous chalcogenide layers and structures. They may serve as a basis for some novel applications for prototyping elements of optoelectronics.

The research on ChG based NLS has started with studies of chalcogenide-chalcogenide structures like Se/As_2S_3, Ge/Se and CdS/Se [10, 11]. Continuing this trend, we devoted our attention to the metal/chalcogenide structures like Sb/As-S(Se) and to the NLS fabricated from Ge-based ChG. First, some additional problems of the fabrication technology were solved. These involved further development of a computer driven vacuum evaporation equipment and application of pulsed laser deposition (PLD) technology. We compared metal/ChG NLS with basic chalcogenide/chalcogenide NLS like Se/As_2S_3, as well as with properties of some component materials in separate layers. These experiments give us new insight into the behavior of glasses at nanoscale, interdiffusion mechanism at nano-interfaces, induced volume changes and parameters of direct surface optical and/or geometrical relief recording. The main interest of our work was the comparison of light- and e-beam relief recording. We found the common characteristics in structural transformations induced by different external sources of energy,and in addition we developed a direct e-beam recording in these materials.

2. Bibliographic overview

2.1. Structure and properties of amorphous chalcogenides

Amorphous materials are characterized by the following features:

1. absence of direction of any feature dependence;
2. arbitrary surface at the edge of breaking;
3. absence of crystalline phases included in the volume.

Amorphous materials, as gases or liquids, are isotropic. Based on electrical properties amorphous solids are classified as metals, semiconductors or insulators. Among these, amorphous semiconductors have attracted considerable attention due to their significance in many diverse applications [12]. The term “amorphous” is frequently used instead of the terms “glassy” or “non-crystalline”. Very often an amorphous material means a metastable thin solid film. It is prepared from a glass which is a viscous supercooled liquid formed by continuous quenching of a melted material. An ideal glass or amorphous material is a solid in the state of internal equilibrium. This equilibrium state is characterized by a definite set of equilibrium positions about which the atoms are continuously oscillating. The determination of the equilibrium state shows that in amorphous materials the distances between atoms have statistically the same magnitude as in the crystalline materials (Figure 1.1).

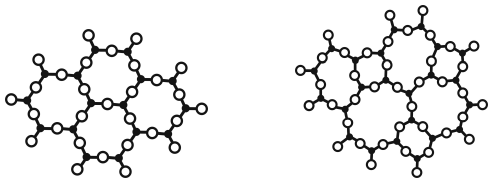

Figure 1.1. Equilibrium ordered states of atoms in crystalline material (a) and in its amorphous phase (b) (after Zachariasen [13]).

Chalcogenide materials are compounds, alloys or composites containing elements from Group IV of the periodic table below oxygen, e.g. sulphur, selenium and tellurium. A focused interest emerged to these materials in a glassy state after investigation of glassy selenium and its semiconducting properties. These were established first by N.A.Goryunova and B.T.Kolomiets in the 1950s for arsenic sulphide glasses which are optically transparent in a wide IR region. In comparison with oxide glasses, these materials are characterized by increased thermal expansion coefficient, increased thermal coefficient of refraction and optical nonlinearity constants, and well defined p–type conductivity. The mechanical properties, thermal and chemical stability of chalcogenide glasses are worse in comparison with oxide glasses. These differences are mainly attributed to the peculiarities of atomic bonding, presence of special defect states and unidirectional chain-like or layer-fragment structural elements [14]. The last specific feature causes some important deviations from the general definition of the glassy state given at the beginning of this chapter. Certain ordering occurs for example under the influence of polarized light [15]. It can be one of the basic moments of directed mass transport, as will be discussed later in more detail.

Binary chalcogen-containing alloys exist both in crystalline and amorphous phase. Glassy compounds in the most investigated As-S(Se) system are produced by melting-quenching technique.

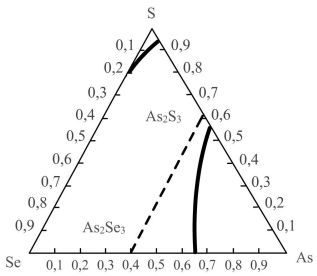

Figure 1.2. Glass formation region in As-S-Se system (after Borisova [2])

They are characterized by a wide glass-forming region, as shown in figure 1.2. Amorphous films are usually prepared by vacuum evaporation, sometimes by magnetron deposition or very rarely by precipitation from solutions.

The glassy (amorphous) state conserves the short range order (SRO) in the 0.3-0.5 nm range. In this range the atomic structure is almost uniform and contains elements of ordered structure of the nearest crystalline counterparts. In the case of dominantly covalently bounded amorphous solids, SRO is described by local coordination polygons, e.g. pyramidal AsS_3 in As_2S_3 or tetrahedral GeS_4 in $GeSe_2$. The coordination number N_c of nearest neighboring atoms, the relative distance and the angles between them describe the topological SRO. It should be mentioned that in this picture of SRO the detailed feature information about interconnections of structural elements is absent. In many amorphous materials, especially in chalcogenide glasses, such order shows up in longer distances. This is the so called medium range order (MRO) which extends up to the 0.5-1 nm range. MRO is defined by the type of interconnections of structural elements and their relative orientation. For disordered materials the long range order (LRO) is absent, e.g. amorphous chalcogenides have no translational symmetry.

The energy band-structure of crystalline materials is a main concept in solid state physics. Electric, photoelectric or optical properties based descriptions of crystalline semiconductors are elaborated in the framework of energy band models. A direct consequence of the translational order is that the allowed energy states form bands, which are separated by regions of forbidden energy states. But amorphous solids lack this kind of order and are only characterized by MRO or SRO. Hence, concepts which are based on the Brillouin zone, the Bloch-function or the periodical potential cannot be straightforwardly transferred to amorphous materials. Nevertheless investigations by Ioffe, Weaire, Thorpe, Mott, Anderson and others revealed that many of the fundamental properties such as the existence of insulators, semiconductors and metallic glasses, the optical absorption edge, the Arrhenius nature of electrical conductivity, etc. are common to both crystalline and amorphous solids [16]. This shows that these physical properties are associated with the SRO and/or MRO rather than the translational periodicity. Anderson's theory assumed [17] and Mott suggested

[18] that disorder in configuration causes spatial fluctuation in potential of amorphous materials, which leads to the formation of localized states. These states, which do not fall into the conduction or valence bands, form tails above and below the valence bands.

Specific models are used to describe glassy behaviors of chalcogenides. A few of them will be briefly reviewed here.

X-ray diffraction patterns are described by atomic-electronic radial distribution function (AERDF), while density, crystallization enthalpy, etc. were first explained by Polk with a continuous random network model (CRN) [19]. The latter approach was further developed by Steinhart *et al*. [20] and Popescu [21]. There are several limitations in both models. The AERDF model is not able to explain the first small sharp diffraction peak observed in amorphous silicon [22] since it does not support large scale growth [23]. In the random network model (RNM) with covalent bonding [24, 25], it is assumed that the distribution of bonding types (i.e. A_xB_{x-1}) can be characterized by coordination numbers N_a, N_b and relative concentrations x and $1-x$ of A and B atoms, respectively. RNM allows creation of A-A, B-B and A-B connections in the whole composition range except when x=0 and x=1. This approach does not take into account the relative bonding energy.

The topological threshold model rests on the basis of the constraint counting model (CCM), proposed by Phillips in an attempt to relate the glass forming tendency in the chalcogenide glasses with the network topology [26, 27]. It was shown that the glass forming tendency is governed by the SRO [28]. This model is applicable to all covalent network glasses, where bonds are highly directional. The most favorable is a glass where the number of constraints (N_c) acting on the glass is equal to the degrees of freedom (N_d). Assuming only the nearest-neighbor contribution, the topological constraints on an atom with r nearest neighbors can be written as:

$$N_c = \left(\frac{r}{2}\right) + (2r - 3), \qquad (1.1)$$

where the first term represents the bond-stretching constraint while the second term the bond-bending. The factor 1/2 signifies that a bond is shared equally between two atoms.

The term of *(2r-3)* means that an atom with a nearest-neighbor coordination of *r* has two bond-bending (bond-angle) constraints. For each of the remaining *r-2* bonds, two bond-angle constraints are specified. Thus, the total number of bond-angle constraints on an atom will be *1+2(r-2)* or *(2r-3)*. For a three-dimensional glass, N_d is taken as 3 resulting in $r = 2.4$. When $N_c < N_d$, $r < 2.4$, the glassy network is under-coordinated (so called floppy). When $N_c > N_d$, $r > 2.4$, the glassy network is over-coordinated (rigid). Hence $r = 2.4$ is referred to as the mechanical threshold. Later Thorpe *et al*. [29, 30] showed that this transition at mechanical threshold can be treated as a percolation, with the percolating quantity being rigidity.

The idea of rigidity percolation has stimulated a lot of experimental and theoretical work to look for such threshold behaviors. On the experimental side, discontinuities in floppy modes have been detected by inelastic neutron scattering, differential scanning calorimetry, elastic constants and sound velocity measurements [31, 32]. However, a few glasses show characteristic change at $r = 2.67$, in addition to that at $r = 2.4$ [33]. To explain such features, CCM was extended to two dimensional layered glass structures. In this modified approach, the constraint balancing equation can be written as $3 = r/2 + (r-l)$ (according to eq.1.1).

The above expression gives $r = 2.67$ as the critical value for a 2D layered to 3D cross-linked structural transition. The arguments presented above assume a network in which the coordination numbers are greater than or equal to two. For a network with one fold coordinated species, the condition for rigidity percolation is given by $r = 2.4 - 0.4\ (nl/N)$, where (nl/N) represents the fraction of 1-fold coordinated atoms. These considerations seem to be useful for explaining photoinduced plasticity and related effects.

Two phenomenological band-models based on the concept of localized states in the band tails were proposed: the Cohen-Fritzsche-Ovshinsky model (CFO) and the Davis-Mott model (DM).

The CFO model [34] describes extensive tailing of band edges. Tailing is envisaged to happen as a result of both compositional and topological disorder. In fact, the bonding is so extensive that they overlap in the mid-gap. As a consequence of the overlap, the states in the tail of the conduction band have lower energy than those in the

tail of the valence band, resulting in positively charged valence band tail states and negatively charged conduction band tail states. The Fermi level is pinned due to this extensive overlap. The tail states are localized due to the disorder and are separated from the extended states in the band at critical energies called the mobility edges. Though the model can explain the pinning of Fermi level, the limited tailing of localized states and the absence of a real gap make it an unrealistic model.

In contrast to CFO model, the extension of band tails in DM model [35] is up to only a few tenths of an electronvolt into the band gap. The concept of mobility edge is retained. In addition, pinning of E_F is believed to be due to a large density of states near mid-gap. These states arise from discrete defects, like dandling bonds present in an otherwise fully connected network.

The CFO and DM models explained the pinning of Fermi level successfully, but failed to explain the absence of electron spin resonance signal and hopping conduction in chalcogenide glasses. Thus, a clear contradiction prevails. E_F is pinned, but, on the other hand, there is no evidence for unpaired spins. Anderson resolved this issue by suggesting that chalcogenide glasses have only paired spins because of the strong electron-lattice interactions [36]. He assumed that it is energetically beneficial for the system when the energy of Coulomb repulsion forces of electrons is compensated by strong two-electron bonding energy (including the lattice deformation energy). These ideas led Anderson to formulate dandling bonds with negative correlation energy. This idea of spin pairing was used independently by Street and Mott as the charged dandling bonds model (CDB) [37] and Kastner and Fritzche in the valence-alteration pairs model (VAP) [38].

The CDB model considers the specific dandling bonds. They can form three states. Neutral state, D^0 is formed when each dandling bond has an unpaired electron. When two electrons or none are located on the bond, the bond is denoted as D^- and D^+, respectively. The coordination number of a chalcogen atom at D^+ is three (overcoordinated), and at D^- is one (undercoordinated). The energy required to overcome the repulsive Hubbard energy (the energy required to place an extra electron in D^0 site in order to form the D^- site) is gained by forming the extra bond at D^+ site. It can be seen from the following considerations

$$\left.\begin{aligned} D^{+} + e(+E_1) &\rightarrow D^{0} \\ D^{0} + e(+E_2) &\rightarrow D^{-} \end{aligned}\right\} \qquad (1.2)$$

Here E_1 and E_2 are the energies required to add an electron to a particular site so that the reaction $2D^0 \rightarrow D^+ + D^- + (E_1\text{-}E_2)$ is accompanied with energy increment. This model explains successfully many experimental results [39].

The VAP gives a description of specific, thermodynamically favored defects which are present in the glass. The number of such defects is denoted as:

$$N = N_0 e^{\frac{-G_f}{kT_g}}, \qquad (1.3)$$

where G_f is the free energy of defect creation and N_0 the number of sites in the solid. In a glass the lowest temperature at which the defects anneal out is the glass transition temperature T_g. Thus, the density of defects depends upon G_f and T_g. In this model the configuration of chalcogen atoms is denoted identically to the CDB model. D^- refers to C_1^- and the D^+ refers to C_3^-, where the C represents a chalcogen atom, the subscript represents the coordination and the superscript the charge state. In the VAP model the lowest energy configuration has a symmetrical C_3^0 centre. The VAP model proposes a reduction of the formation energy for VAPs, if they are formed very close to each other with Coulomb energy of attraction. Such pairs of VAPs are called intimate valence-alternation pairs (IVAP). While VAP constituents are random C_3^+ (or D^+) and C_1^- (D^-), IVAP constituents are nonrandom C_3^+ (or D^+) and C_1^- (or D^-).

An alternate approach to understanding the origin of bandgap in amorphous semiconductors is the chemical approach or the tight-binding approximation methods [40] put forward by Kastner [41], Ovshinsky [42] and Kastner, Adler and Frtizsche [43]. It is equally applicable to both crystalline and amorphous solids since the model depends only on the short range order. The nature of bonds, coordination number and their valence state are the main factors on which the general nature of density of states

depends in solids. The discrete energy levels of each atom are split into bonding and antibonding states which form bands due to the interaction between the neighboring atoms. In a-Se, the lone-pair orbitals form the upper part of the valence band and the empty antibonding states form the conduction band. As compared to the valence band, the bonding states are lowered in energy, while the antibonding states are raised in energy [41]. Because of the lone-pair origin of the valence band, chalcogenide glasses are often referred to as lone-pair semiconductors.

The structure of materials, such as the structure of non-crystalline tetrahedral bonded semiconductors, is governed by the thermodynamics of the system and depends on the energy, duration and time of excitation, or perturbance. The system is effectively forced to search for a minimum energy state on a progressively smaller spatial scale. The thermal vibrations and diffusion processes allow changes in bonding and therefore the topology of the atomic network is altered.

For nanolayered samples, significant attention should be given to diffusion processes between constituent layers. Driving force, mechanism and behavior of interdiffusion of chalcogenide layers highlight new possibilities, features and applications for new functional materials, items and devices. Some features could be approached only by developing nanolayered chalcogen structures.

Materials and thin film structures, based on As_2S_3, GeSe, GeS systems and Se, Sb are investigated in detail in the present work in connection with induced structural transformations. It is worth mentioning that the structure and properties of chalcogenide glasses are weakly dependent on preparation conditions (e.g. T_g of bulk corresponds the same value of T_g for thin film) and annealing, as in case of other non-crystalline semiconductors [44, 45].

2.2. Induced structural changes

It was noticed in the early beginning of investigations of the amorphous chalcogenides that during external excitations like irradiation by light or electron beam, the optical, chemical and electrical properties of the samples show changes. Such changes were dependent on the nature of the excitation source, such as light flux, wavelength or the temperature of the sample. After annealing at temperatures close to the T_g, the induced changes usually disappear, so they can be considered as reversible processes. In contrast, crystallization of an amorphous material can be considered as an irreversible structural change similar to the densification, structural changes of the freshly deposited amorphous films, which are in a highly metastable state. At the same time crystallized spots in a layer can be re-amorphysed by appropriate pulsed heating (illumination), as happens in rewriteable optical discs.

Photoinduced crystallization and appropriate changes of electrical and optical parameters are the most dramatic phenomena observed in chalcogenide amorphous semiconductors. These phenomena appear to be induced electronically or thermally and can be observed easily in Ge-Te-Sb or similar alloys, used in R- or RW DVD, or Ovonic switch [46].

The number of covalent bonds interchanged in the photo-crystallization process seems to depend upon the material of interest. In amorphous Se which is composed of distorted chain molecules [47, 48], interchange of a few atomic bonds (~1%) seems to be sufficient to align the distorted chains into hexagonal crystals. Breaking of covalent bonds and reptile motion of chain fragments are probably needed, like the crystallization process in chain polymers [49]. In contrast, in a ternary compound like Ge-Sb-Te [50], bond breaking and reconstruction of a greater number (~10%) of bonds may be needed to produce polycrystals, since compositional disorder is inherent in these compound materials. In Ge-Te-Sb alloys the reversible cycles of crystallization-amorphyzation are connected with changes in Ge atom position within short-range ordered structural units.

Photo-induced reversible changes of optical, mechanical and chemical parameters in As-S(Se) based materials, as well as in some Ge-based and other multicomponent chalcogenide glasses, are not as dramatic and theoretically evident as crystallization, although they serve as a basis for different optoelectronic applications. Photo-induced reversible changes seem to be a great challenge for theoretical descriptions. Up to now intensive investigations have been performed in this direction and no clear models are available.

2.2.1 Photoinduced structural changes

Light interaction with chalcogenide glasses significantly differs from interaction with crystalline semiconductors. Irradiation of crystalline semiconductors and insulators with light that corresponds to band-gap wavelength can influence only the electron configuration. The produced electron-hole pairs contribute to the electrical response of the material (photoconductivity, evolving of photoelectric force). Such excited carriers can recombine either radiatively or non-radiatively.

Contrary to the crystalline semiconductors, the incidental light also influences significantly the atomic structure of the chalcogenide glasses. This is manifested in unique behavior of these materials such as photo-induced changes. Non-radiative recombination of the excited electron-hole pairs can leave the material in a state which is different from the initial state. The near band-gap light irradiation could initiate structural changes which remain after irradiation for several weeks or much more at ambient conditions. Such phenomena were observed in absorption edge [51], refractive index change [51], volume change [52], solubility, elasticity, etc.

The absorbed light significantly influences the rate of atomic displacement in chalcogenides. Thus, the viscosity of this glassy material decreases, while [53, 54] the diffusion of atoms increases [55]. The main interest of the investigation was focused on optically induced volume changes, solubility changes and induced diffusion of silver, since they can be used for lithography, data recording and photonic applications [56-59].

Shimakawa classified the photo-induced effects into structure related photo-induced effects and defect related effects [60]. The defect related photoinduced effects are mid-gap absorption, decay of photoconductivity, photoluminescence fatigue and light induced electron spin resonance. The structure-related photoinduced effects include photo-darkening, photo-crystallization (or amorphyzation), photopolymerization, photo-contraction or photo-expansion, photo-dissolution or diffusion and photo-induced fluidity.

The photo-induced structural changes can be reversible or irreversible. The reversible structural changes are observed on thin film or bulk samples pre-annealed at T_g temperature. After several hours of annealing, the sample returns to initial state. This is the so called “erasing”. During repeated irradiation the changes occur again, which can be erased by subsequent annealing. Such cycles can be repeated an arbitrary number of times. The sample behavior does not depend, or depends only slightly, on the preparation method, but it does depend on the sample composition, the irradiation conditions and thermodynamic parameters. In contrast, the freshly prepared (not annealed) sample behavior significantly depends on the sample preparation conditions. In this case the annealing doesn’t return the system completely into initial condition. Therefore, such structural changes are considered to be non-reversible or partially reversible. It is almost a commonly accepted statement that reversible photo-induced changes are macroscopically athermal, i.e. no essential (in comparison with annealing at T_g) heating occurs during illumination, although microscopically the thermal spike model [61] can be successfully applied to these processes and even to the photo/induced interdiffusion [62].

2.2.2 Electron-beam induced structural changes

Electron beam irradiation is a kind of corpuscular irradiation. The main mechanisms of electron interaction with matter are electromagnetic interactions with atomic electrons (ionization and excitation) and with Coulomb field of the nucleus. The scattering process on a nucleus exists when an electron penetrates through the matter. In cases when the electron energy is higher than the threshold energy of an atomic displacement T_d, an atom can be shifted. But the probability of this shift is rather small in comparison with ionization and excitation. In general, ionizing irradiation in solids can cause radiation defects with atomic displacements [63]. The energy is the most important parameter of such irradiation.

The dose indicates the number of induced radiation defects in the irradiated sample. In general the absorbed dose is denoted as:

$$D_n = \frac{\Phi_e}{\rho}\frac{1}{h}\int_0^h \frac{dE}{dx}dx, \qquad (1.4)$$

where Φ_e the fluence of electrons, ρ the sample density and h the sample thickness, dE/dx is the electron energy loss per unit path length.

The threshold energy of an atomic displacement T_d in crystalline chalcogenides with strong covalent bonds ranges from 5 to 10 eV. [64]. In amorphous materials this energy is less than the above mentioned quantity for specific structural reasons. Thus during irradiation by electron beam with the energy of 2.8 MeV, fluence 10^{16}-10^{17} cm^{-2}, approximately 10^{19} cm^{-3} displacement defects are created. The number of defects reaches several percents of all atoms.

After electron beam irradiation with the energy of 20 keV, a significant shift of the band gap to the longer wavelength range and a decrease of the transmittance (darkening) were observed in amorphous As_2S_3 [65]. The magnitude of the observed effects depends on the density and duration of the electron beam irradiation. It was

explained by structural reorganization of molecular components, just as by breaking and formation of new chemical bonds [66].

Irradiation of samples of an As-S chalcogenide system by electron beam causes some decrease in the intensity of photoluminescence. It follows that irradiation induced creation of additional deep defect centers occurs analogously to the bond breaking ones. Philips explained [67] this mechanism by the presence of micropores and microspaces in the sample. On the boundary of interfaces of the micropores and microspaces, a recombination process can take place. During irradiation these pores are growing, so the boundary surface is increasing, thereupon increasing the recombination rate.

The role of compositional dependence is also worth mentioning. The most significant optical changes were observed in $As_{40}S_{60}$ and $As_{44}S_{56}$ thin films [68]. The observed effects are explained by As-As homopolar bonds which create a localized antibonding energy state. The probability of creation of such a state increases with increasing As concentration. Therefore, the increasing number of acts of charge carrier localization during electron beam excitation influences the valence band. Eventually the related induced effects (optical, for example) are enhanced. After annealing, the samples return to the initial state.

2.2.3 Induced interdiffusion

Photoinduced diffusion of elements is a very important effect in amorphous chalcogenides. The effect was first observed by Kostyshin et al [69]. They observed large dissolution of certain metals in chalcogenides under light irradiation. The photoinduced diffusion is exhibited by Ag, Zn, Bi and Se. The mechanism of photoinduced diffusion for different elements may be different [70-72]. Among photoinduced diffusion processes the most notable is the behavior of Ag in As-S, Ge-S and Ge-Se glasses. On exposure to light, Ag atoms diffuse into the glass as Ag^+ ions. Ag diffusion is particularly affected by the light quantum of band-gap energy, but can also be induced by sub band gap light. The aforementioned diffusion is due to the

chemical or intercalation reaction between the glass and Ag which in turn is enhanced by the light absorption at the doped-undoped regions [73]. The driving force for the reaction is the electrochemical potential gradient for Ag, and the kinetics is facilitated by the photogeneration of electrons and holes.

A very important photo-induced effect in amorphous chalcogenides is the photoinduced interdiffusion. The effect was first observed by Kostyshin et al [74]. Except for the photo-diffusion of silver, we have very little information on light induced atomic transport processes in amorphous chalcogenide [75, 76]. Studies on interdiffusion could provide a better understanding the problem of diffusion in amorphous semiconductors. Although studies on interdiffusion in chalcogenide NLS were made by several authors [77-79], this question seems to be still unsolved.

2.3. Amorphous chalcogenides as elements of photonics

The unique properties and behaviors s of amorphous chalcogenides such as wide optical transmission band in *IR* spectral region, large glass forming region, metastability, photoinduced changes of mechanical, electrical and optical properties, photoconductivity etc., make them excellent materials for photonic applications. Many authors have intensively investigated these materials and have described them as materials for integrated optics [80], waveguides [81], holographic memories [82], ultrahigh-density optical storages [83] or phase change optical storages [84, 85]. Amorphous selenium is a classic material for Xerographic applications [86] and has recently been highlighted as a promising photoconductive material for digital X-ray radiography [87]. Furthermore, amorphous chalcogenides include potential for improving and expanding the range of applications.

Up to now chalcogenides have been used in numerous devices and applications. Since the discovery of Ovonic memory switching laser recording phase-change memories have been rapidly developing. A multilayer combination of GeSbTe and Sb allows us to obtain less than 100 nm optical resolution due to electromagnetic field interaction between optical near-field and surface plasmons generated on the films. Optical devices on micro and nanoscale are available as diffraction gratings, holographic gratings, focusing or Fresnel lenses and witches. In the field of information technology the development for telecommunication related devices like fiber based applications can be mentioned in addition to high density data storage.

Generally the chalcogenide based nanostructures are created in a sequence of several writing, patterning, irradiation and etching steps. Main emphasis is put on the methods and technology which lead to the desired application, effect or device. In this respect in the present work one-step methods of fabrication and developing structures and/or property-changes on definite elements are presented.

For fabrication of photonic elements, light and electron-beam treatment appeared to be optimal in terms of simplicity of technology and wide industrial demands. Photo-induced changes are excellent possibilities to create bigger patterned

areas in one step. Although the size is limited by diffraction, the method can be applied in the creation of diffraction and holographic amplitude, phase gratings, or even optical data carriers. Additionally, electron beam treatment gives a powerful possibility of creating complex and unique patterns. These two possibilities will be discussed in more detail in the present work.

3. Sample preparation technology and experimental techniques

3.1. Sample preparation

Chalcogenide bulk glasses are generally prepared by melt-quench technique from predefined components in a vacuum sealed quartz ampoule. High purity elemental components are placed in the necessary proportion into the quartz ampoule. After sealing, the synthesis occurs at the appropriate high temperatures, the melt is cooled down and the quality of glass is checked by standard structural analysis. For the preparation of thin layers, these bulk materials are used as origin materials. The most common technique for the production of amorphous thin layers is the thermal vacuum evaporation (TVE). The advantage of this technique is its simplicity and the low cost of operation. Target materials are usually evaporated under high vacuum, 2×10^{-5} mbar, from current-heated tantalum or tungsten boats. Corning glass, micro slide glass, or face down polished silicon wafers are used for substrata.

With TVE method we prepared multilayered samples by using computer controlled rotating sample holder which allowed us to change the position of the substrata above the targets. The targets were well isolated from each other in a common vacuum chamber together with the sample holder-positioning system. The step-motor driven sample positioning system and shutters were computer controlled, too. The modulation period was varied by choosing the delay time spent above the appropriate evaporated target. The purity of used bulk glasses was at least 99.999%.

Pulsed laser deposition (PLD) is another prospective deposition method. It is favorable because of its simplicity, easy control of the process and of stoichiometric transfer of target material to the films. PLD technique is also applied to fabricate films of unusual composition [88]. It is worth noting that the latter requirements can not be always ensured by thermal evaporation technology, especially for more complex glasses, or Ge containing glasses with high evaporation temperatures.

A KrF excimer laser (Lambda Physik COMPex 102) operating at 248 nm with constant output energy of 250 mJ per pulse, with pulse duration of 30 ns and with repetition rate of 10 Hz, was used for PLD. The energy fluence on the targets was held constant at 1.4 J cm^{-2}. NML were deposited in a vacuum chamber at background pressure less than 2×10^{-5} mbar. For PLD substrates, we used chemically cleaned microscope glass slides positioned parallel to the target surface. Target to substrate distance was 5 cm. In order to obtain thin films that were as homogeneous as possible, the off-axis PLD technique with rotating substrates, in combination with scanning of ~1×1.2 cm^2 targets by the laser beam, was used. The selected period of a bilayer was chosen to 9 nm or less with $d_A/d_B \approx ½$, where d_A and d_B are the deposition rates of *A* and *B* components, respectively. Knowing the individual deposition rates for *A* and *B* components, the total thickness of the NML was expected to be close to 1 μm.

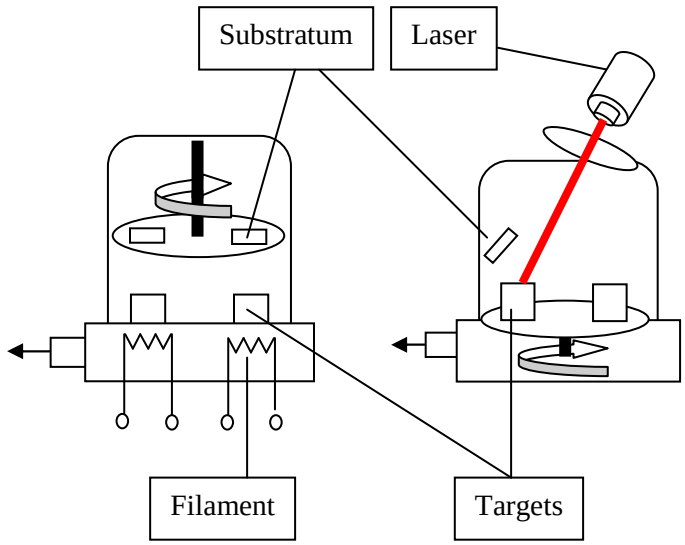

Figure 3.1. TVE (left) and PLD (right) sample preparation techniques

3.2. Optical measurements

Optical transmittance spectra were measured by Shimadzu UV-3600 spectrophotometer in the wavelength range from λ = 250 nm to 2000 nm. Kinetics of the photoinduced optical changes was measured *in situ*, as described below.

Optical measurements give information about the optical properties of the samples. In optical measurements the main parameters of interest are the refractive index *n*, the absorption edge referring to the optical band gap E_g, the absorption coefficient α and the thickness of the sample *d*. I have determined these optical parameters from the obtained transmittance spectra using Swanepoel method [89]. Additionally, these parameters were also determined by ellipsometric measurements with variable angle spectroscopic ellipsometry (VASE, J.A. Woollam Co., Inc.) in the spectral range of 500-2300 nm at 65°, 70°, and 75° measuring angles of incidence. The total thickness of the samples was easily determined by profilometer or AFM.

Transmittance spectrum is taken for the determination of optical parameters. The found general trend is shown on figure 3.2. As it can be seen from the figure, the transmittance spectra can be divided into four - strong, medium, weak and transparent - absorption regions.

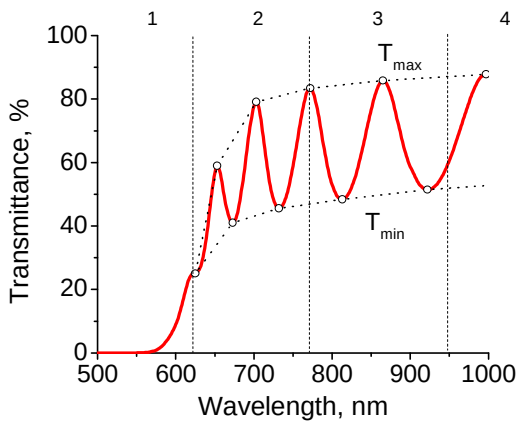

Figure 3.2. Transmittance spectrum of a thin layer

Optical transmittance is limited from the low energy side by phonon absorption and from the high energy side is limited by absorption edge; the optical absorption below $\alpha < 2\times10^4$ cm^{-1} provides information about density of states in the band tails. Since the activation energy of amorphous chalcogenides corresponds to $\alpha = 10^4$ cm^{-1}, M. Stuke proposed to determine the optical band gap by this value of optical absorption coefficient. Such measurements correlate well with results of photocurrent measurements. According to Tauc [90] the optical absorption in region above $\alpha \geq 10^4$ cm^{-1} is influenced by electron transitions from delocalized states in the valence band ($E \leq E_v$) to the delocalized states in the conduction band ($E \geq E_c$). The frequency dependence of the absorption coefficient with respect to a constant value A is given by a parabolic approach:

$$\alpha(\omega) = \frac{A[h\omega - (E_c - E_v)]^2}{h\omega}. \qquad (3.1)$$

The absorption coefficient is calculated from the transmittance spectra according to the following thinking. When a monochromatic beam of light is incident on a medium at a normal incidence then:

$$T = \frac{(1-R)^2 e^{-\alpha d}}{1-R^2 e^{-2\alpha d}}, \qquad (3.2)$$

where R is the reflection, the T is the transmittance, n is the refractive index, α is the absorption coefficient and d is the thickness of the material through which light passes. Since $exp(-2\alpha d)$ much less as $exp(-\alpha d)$ equation 3.2 can approximately be expressed as:

$$T = (1-R)^2 e^{-\alpha d}, \qquad (3.3)$$

From transmittance spectra (when no reflection is given) the absorption coefficient could be obtained from the formula:

$$T = T_0 e^{-\alpha d}. \qquad (3.4)$$

This formula is valid for $\alpha \geq 10^{-3}\text{cm}^{-1}$. A more convenient calculation of optical parameters of thin layers was made from a transmittance spectrum using the method of Swanepoel [91, 92] described above.

In the region of weak and medium absorption from positions of fringes the refractive index n* can be calculated according to the equation (3.5), where *s* is the substrate refraction index, T_{max} and T_{min} the appropriated transmission maximum and minimum of the given fringe.

$$n^* = \left[M + \left(M^2 - s^2\right)^{1/2}\right]^{1/2}, \qquad (3.5)$$

where

$$M = 2s\frac{T_{\max} - T_{\min}}{T_{\max}T_{\min}} + \frac{s^2 + 1}{2}. \qquad (3.6)$$

The sample thickness is given from the next equation:

$$d^* = \frac{\lambda_1\lambda_2}{2(\lambda_1 n_2 - \lambda_2 n_1)}, \qquad (3.7)$$

where λ_1, λ_2 and n_1, n_2 are the corresponding wavelengths and refraction indexes for T_{mat} and T_{min} respectively.

The latter equation is very sensitive to errors in refractive index. Using the $2nd=m\lambda$ expression for each *n*, the thickness d of the sample can be calculated. Finally, by averaging the thickness can be obtained with 0.2-0.5% accuracy. Even better results can be achieved by direct thickness measurement using a laser profilometer, type Ambios XP-1. For this reason, the vacuum evaporator was equipped with two control

samples above both evaporator sectors. Thus, the thickness of control samples corresponds to the total thickness of the given material in the nanolayered structure.

Laser irradiation was performed according to a scheme shown in figure 3.3.

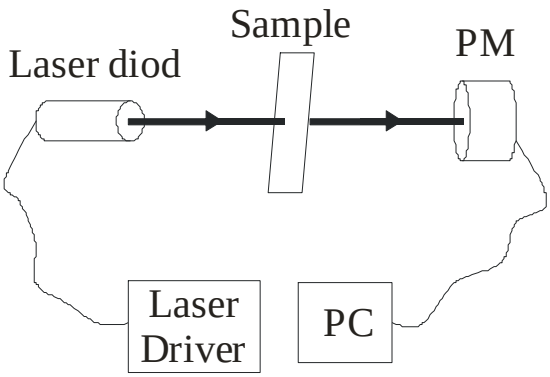

Figure 3.3. Laser irradiation setup

Illumination was made by different lasers modules and laser diodes from ThorLabs with different intensities, polarizations and wavelength (exact wavelength mentioned below). The light intensity was measured in-situ by PM120 ThorLabs optical power meter connected to a personal computer.

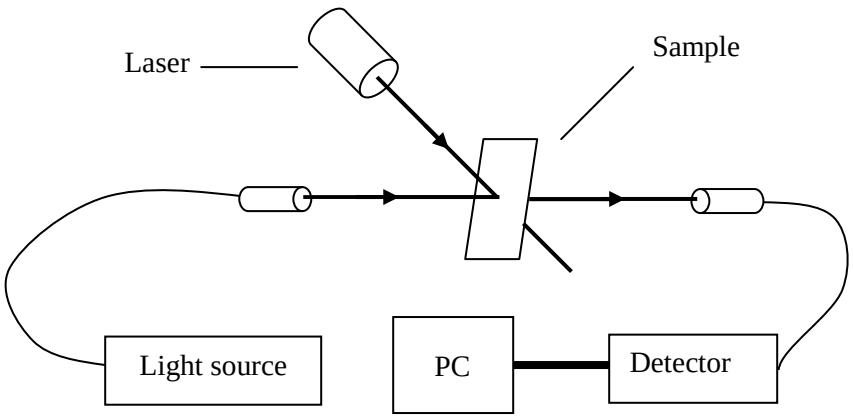

Figure 3.4. Schematic presentation of *in situ* spectrometry during laser irradiation

Measurements of photoinduced transmission change were performed also by OceanOptics millisecond spectrometer (fig.3.4.). The transmission was recorded at millisecond/record rate during the whole period of illumination in the visible spectral range.

Modulation period of the multilayers was determined with the help of control samples placed directly above the evaporation sources. The results were checked by low angle X-ray diffraction (LAXRD) measurements which additionally give information about the quality of the interfaces, as well (see below).

3.3. X-ray diffraction measurements

The X-ray diffraction technique is a widely used method for investigations of multilayered structures. It is a non destructive method which gives information from the atomic scale range. From a methodological point of view two regions are distinguished regarding the X-ray angle of incidence: the region up to 15° is called low angle X-rays diffraction and the range above 15° - small angle X-ray diffraction.

Using the low angle spectrum the spatial resolution exceeds the lattice size. Thus, the X-ray spectrum is independent of system constituent components of atomic structure, which makes possible the investigation of chemical modulation of the system. At the modulation period Λ of a multilayered structure the reflection gives sharp higher order peaks which correspond to the Bragg reflection according to the formula:

$$\sin^2\theta = \left(\frac{n\lambda}{2\Lambda}\right)^2 + 2\delta, \qquad (3.8)$$

where θ is the angle of incidence, n the reflection peak order, λ the X-ray wavelength, $1\text{-}\delta$ is the real part of the refractive index of the superlattice [93].

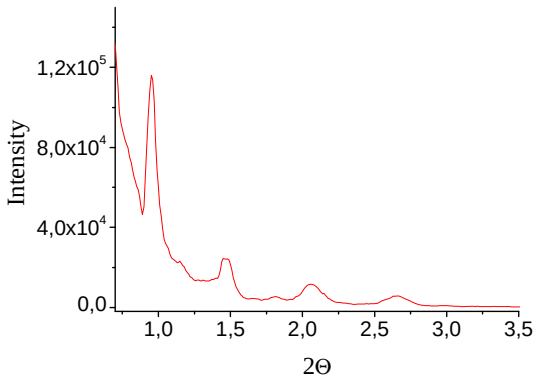

Figure 3.5. LAXRD spectrum of nanolayered sample Se/As_2S_3

Using this technique the quality of the interface and the modulation period can be determined. The period of the multilayer or the refractive index is determined through a linear fit of n^2 vs. $sin^2\theta$. The intensities of the Bragg peaks depend also on the sharpness

of the interfaces. Using these features, the LAXRD can be applied to the investigation of diffusion in layered structures due to light or heat treatment. The basic idea of measurement is that during diffusion the interfaces are vanishing which decreases the initially high electron density difference. A typical example is given in figure 3.5. On the graph the intensity of the reflected beam is represented vs. the θ angle of incidence. The following information can be obtained:

- the critical angle (usually around tenths of degree) – a smaller incident angle, at which the detector is saturated as the incident radiation almost directly gets into the detector;
- modulation period (Λ) – the thickness of two different multilayers (thickness of one bilayer) which is determined from the Bragg reflection conditions;
- film thickness – determined from fringes before first order peak;
- fluctuation of the layer thickness – the full width at half maximum of the first order peak is an indication of the quality of the layer, sharp peaks indicate a good thickness repetition, wide peaks indicate the opposite;
- roughness of the interfaces – in the case of investigation of the diffusion in multilayers, the first order peak is taken into account; its intensity indicates the roughness of the interfaces;

The small angle X-ray diffraction spectrum is appropriate for the determination of the structure within a layer. In this region wavelength difference is comparable with the lattice size of the material. The peak positions can be described by the formula:

$$\frac{2\sin\theta}{\lambda} = \frac{1}{\bar{d}} \pm \frac{n}{\Lambda}, \qquad (3.9)$$

where n is the order of main Bragg-peak satellites, $d=\Lambda/N_a+N_b$ is the mean lattice-plain distance, N_a and N_b are the lattice-plain distances of A and B materials respectively. The directly achievable data from the peak position are $\bar{d}$ and Λ. As the X-ray intensity does not contain any information regarding the phase, in order to estimate the lattice parameters or the super-lattice defects of the constituent matter, models should be created.

3.4. XPS measurements

Photoelectron spectroscopy is an excellent technique for probing atomic and molecular electronic energy levels. When an atom or molecule is subjected to high-energy radiation, photons in the radiation collide with and eject electrons from atoms, leaving behind ions. Ejected electrons depart with different velocities. Photoelectron spectroscopy measures the velocity distribution of the released electrons. The kinetic energy, E_k of photoelectrons is equal to the difference between the photon energy $h\nu_{ph}$ and the ionization energy E_{ion}, which is the energy required to completely remove an electron from an atomic energy level:

$$E_k = h\nu_{ph} - E_{ion}\,. \qquad (3.10)$$

A typical XPS spectrum is a plot of the number of the electrons as a function of their binding energy. The peak of binding energy is characteristic for each element. The peak areas are used to determine the surface composition of the materials. XPS is also a useful surface analytical technique to study the chemical state and local environment of an atom. The chemical bonding is often realized through correlation with chemical shifts in XPS binding energies of corresponding elements.

In the present work X-ray photoelectron spectra were acquired by a Scienta ESCA-300 spectrometer using a monochromatic Al K_α X-ray (1486.6 eV) source. Data analysis of XPS spectra was performed by CasaXPS software.

3.5. Raman and IR spectroscopy

Vibrational spectroscopy involves the study of photons that induce transitions between vibrational states in molecules and solids. These transitions typically fall in the IR frequency range. Raman-spectroscopy is used to study vibrational, rotational and other low-frequency modes in a system. A vibrational transition is induced when an incident optical photon of frequency $h\nu_{inc}$ is absorbed and another optical photon $h\nu_{emit}$ is emitted according to the formula:

$$E_n = \left| h\nu_{inc} - h\nu_{emit} \right|. \qquad (3.11)$$

The frequency difference is given by $|\nu_{inc}-\nu_{emit}| = |n' - n''|\ \nu_0 = \nu_0$ since the infrared selection rule $\Delta n = \pm 1$. Two cases can be observed. When the frequency of an emitted photon is shifted to low frequency, $\nu_{inc} > \nu_{emit}$, the final vibrational state of the molecule is more energetic. This shift in the frequency is designated as a Stokes shift. When $\nu_{inc} < \nu_{emit}$, the case is designated as an anti-Stokes shift. Infrared active vibrational modes arise from a change in the electric dipole momentum μ of the molecule, while Raman-active vibrational modes involve a change in the polarizability $P = \mu_{ind}/E$, where the electric vector E of the incident light induces the dipole momentum μ_{ind} in the sample. Thus, some vibrational modes are IR-active, that is, measurable by infrared spectroscopy, and some are Raman-active.

In the present work Raman-spectra were measured on samples prepared by different methods with the same composition and the aim was to compare and make conclusions about the similarity of their structures. Raman-scattering spectra were recorded at room temperature with the Raman-spectrophotometer Bruker IFS 55/FRA 106 using a backscattering method with Nd:YAG laser (1064 nm) as the excitation source.

3.6. Scanning Electron Microscopy and electron-beam lithography

As an electron beam can induce changes in chalcogenides, all the measured samples were scanned at low accelerating voltage covered beforehand by thin conductive layer, typically gold layers sputtered in argon gas.

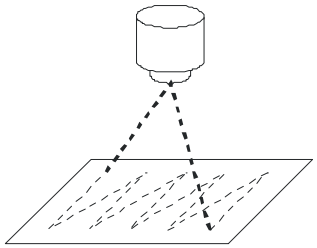

Figure 3.6. E-beam lithography

Electron beam patterning was preformed by a scanning electron microscope type LEO 1550 VP FE, equipped with nano-pattern generator software. Using an electrostatic beam-blanker, the pattern was written digitally, in a dot-by-dot manner, scanning the writing field. At 30 kV accelerating voltage and 750 pA current, the beam was focused to an approximately 1 nm diameter spot. Patterns were written at 30 Pa pressure of nitrogen gas.

To form special unique patterns, a supplemental program was written in addition to the basic nano-pattern generator software. Using this program, Fresnel lenses could be fabricated in a wide range of grey-scale, etc. The main window of the program developed for pattern generator is presented in figure 3.7.

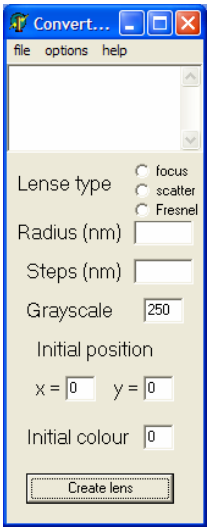

Figure 3.7. Main window of the lens fabrication program

3.7. Atomic Force Microscopy measurements

The Atomic Force Microscope (AFM) is widely used for the investigation of the surface topology. It is a non destructive method which gives a 3-D projection of the surface with high resolution. The AFM does not require special sample treatments and all measurements can be made at ambient conditions. These condition free measurements are an excellent opportunity regarding chalcogenide materials.

During our studies most of the scannings were performed in a contact mode. The *in situ* irradiated samples were scanned in tapping mode.

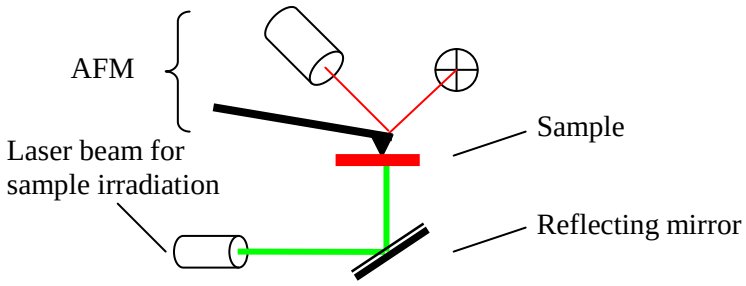

Figure 3.8. Scheme of *in situ* illumination under *AFM*

Surface topography was investigated by Digital Instruments DI-3000 scanning probe microscope and Solver P7 atomic force microscope.

To investigate the magnitude of the volume change, a diffraction pattern was written onto the sample surface using a micro mesh filter. Schematic drawing of the experimental setup is shown on figure 3.9.

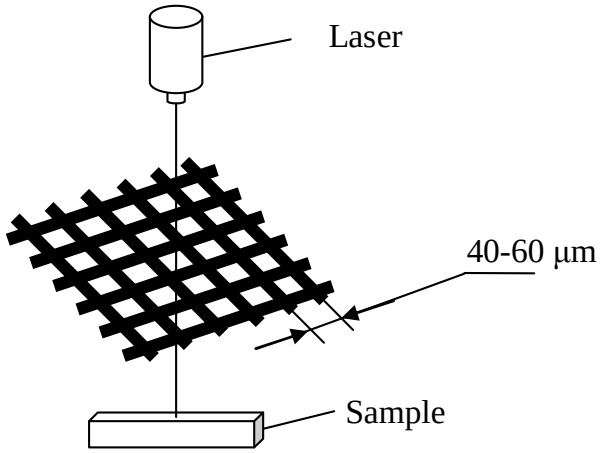

Figure 3.9. Experimental setup of diffraction pattern writing

4. Results and discussion

4.1. Photo-induced changes in layers and layered structures

Chalcogenide glasses undergo photostructural changes induced by light exposure, as it was discussed earlier. Photodarkening is observable in single layers of amorphous selenium or amorphous As_2S_3, while photo bleaching occurs in layered structures. In this chapter we present results concerning the similarities and differences in photo-induced changes of components like Se, As_2S_3, $As_{20}Se_{80}$ single layers and of the Se/As_2S_3, Sb/As_2S_3, In/As_2S_3, $Ge_{20}Se_{80}/Ge_{33}S_{67}$ (further denoted as GeSe/GeS) multilayers.

Two basic statements are established and will be further used regarding amorphous state: the non-crystalline structure does not influence the nature of solid state in terms of the optical absorption and thus the band structure of amorphous chalcogenides does not change while the coordination number is the same; the absence of LRO causes the appearance of band tails in the band gap of localized states near the valence and conduction bands as well as near the Fermi level and it can be changed by external influences [12].

These can be applied to the amorphous selenium, the most investigated non-crystalline formation among amorphous chalcogenides. Thin layers can be prepared by different vacuum evaporation or sputtering methods, so it is evident to use this material and structures with Se as a reference. We used the simplest but efficient thermal evaporation in vacuum. Selenium has several crystalline and non-crystalline allotropic formations. Thermodynamically the most stable is the Se_n spiral polymer chain consisting of trigonal selenium. During annealing all other formations are transformed into the trigonal selenium, and the illumination caused crystallization also can be explained this way [1].

During investigation several samples were made and prepared by methods listed below in the table (Table.1.).

Sample	Preparation method
Se	TVE, PLD
As_2S_3	TVE, PLD
$As_{20}Se_{80}$	TVE, PLD
$As_{40}Se_{60}$	TVE
$As_{50}Se_{50}$	TVE
Se/As_2S_3	Cyclic-TVE, PLD
Bi/As_2S_3	Cyclic-TVE
Sb/As_2S_3	Cyclic-TVE
In/As_2S_3	Cyclic-TVE
Au/As_2S_3	Cyclic-TVE
$Ge_{20}Se_{80}/Ge_{33}S_{67}$	PLD

Table.1. Used samples and preparation methods

A weak photodarkening effect is observable in amorphous selenium films after irradiation at room temperatures. At first it was observed at low temperatures only [94, 95]. Later this phenomenon was observed at room temperature as well, and usually is reversible after annealing the sample near $T_g \approx 310$ K [96]. Photodarkening effect is found to be increased with the level of initial disorder as a result of a photostructural transformation which leads to the broadening of the band tails and hence to the red shift in the absorption edge. Therefore, we used a-Se and a-Se containing NML-s as reference materials in our experiments

The most fascinating photoinduced effect in the mulicomponent amorphous chalcogenides is the reversible photodarkening effect, accompanied with changes of the refractive index. This effect is observable in all arsenic containing compounds and strongly depends on the illumination wavelength: the optimum one corresponds to the absorption edge ($h\nu = E_g$). The most efficient method to follow optical quality (first of all the spectrum and value of α, as well as optical scattering) and the photoinduced changes is the measurement of the optical transmittance spectrum, as it was used in our experiments.

The optical parameters of chalcogenide multilayers as composites depend on the periodicity, parameters of the appropriate sub-layer, and their thickness. Thus, in this work the quality and modulation period of nanolayered structures was first checked by a non-destructive method of LAXRD before the optical measurements. Likewise transmittance spectrum has been taken in order to determine the optical absorption edge, optical transmission band and index of refraction according to considerations already mentioned in chapter 3.2. It should be noted here that refractive index used for multilayered samples is an average complex refractive index of the whole sample according to Cauchy dispersion formulae, i.e. $n = A + B/\lambda 2 + C/\lambda 4$, where n is the refractive index, A, B and C are constants, λ is the wavelength. Thus assuming that the NLS can be ascribed to a single layer with optical properties being average of the individual nano-structured layers.

For comparison, we have measured optical spectra of the basic chalcogenides used in our work. An example for single, d = 800 nm thick a-Se and $As_{20}Se_{80}$ layers is presented in Fig.4.1

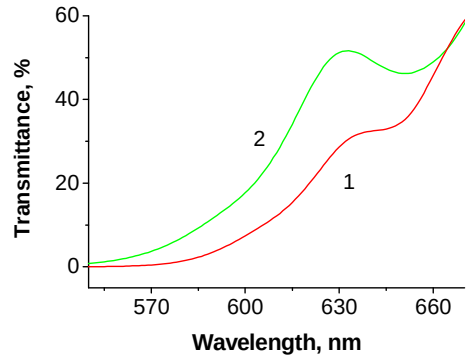

Fig.4.1. Optical transmission spectra of a-Se (1) and of $As_{20}Se_{80}$ (2) layers.

A single layer of pure a-Se has some experimental disadvantages such as ageing effects which lead to the crystallization. The last can also happen under intensive illumination. The best and simplest way to increase the stability of the Se-based glasses is to introduce arsenic in concentration above 2 at% [2]. $As_{20}Se_{80}$ is an excellent example of the rather well investigated stable chalcogenide. The glass transition temperature of $As_{20}Se_{80}$ is at T_g= 104°C [97]. As an example, the

photostimulated change of transmittance of $As_{20}Se_{80}$ composition is shown in figure 4.2. The as-deposited sample was irradiated by P = 5 mW He-Ne laser (λ = 630 nm) for two hours. A long-wave shift is observable in the transmittance spectrum of the irradiated sample. After annealing of the sample at glass transition temperature (T_g) the photodarkening process becomes reversible.

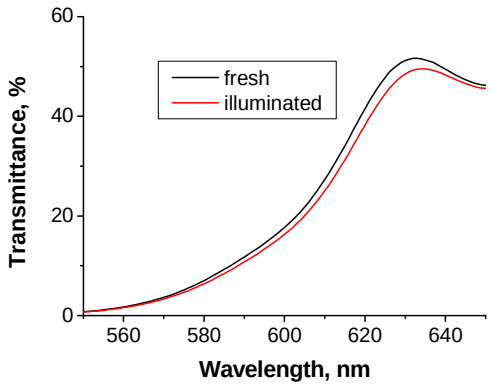

Figure 4.2. Transmittance of $As_{20}Se_{80}$ irradiated by P = 5 mW He-Ne laser light for 2 h at ambient conditions

It should be mentioned that the reversible photostructural transformation occurs only in pre-annealed samples. In the case of as-deposited thin layers the system returns to somewhat higher energy state after an illumination-annealing sequence. However, the continuous illumination – annealing sequences are reversible. Annealing causes relaxation of the disordered state. The duration and temperature of annealing is a significant parameter and varies for different materials or samples.

As it can be seen in figure 4.3, the illumination of the As_2S_3 by the appropriate wavelength laser light (which corresponds to the wavelength of the absorption edge) is accompanied with a shift of the absorption edge (red-shift) (fig.4.3. b), i.e. shrinkage of the band gap and reaches several percents.

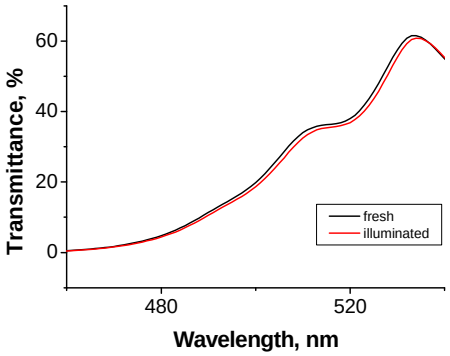

a)

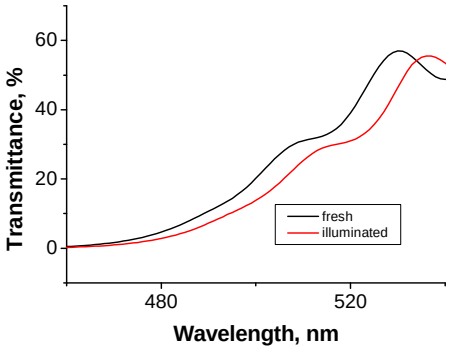

b)

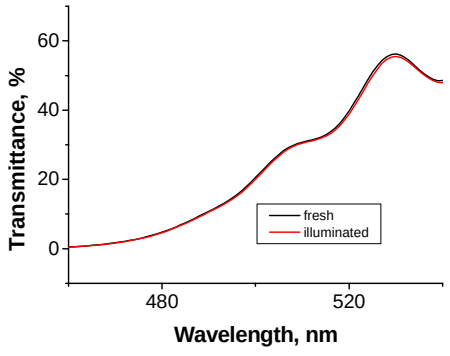

c)

Figure 4.3. Transmittance of As_2S_3 illuminated by a) λ = 405 nm, b) λ = 523 nm, c) λ = 632 nm wavelength laser lights

Meanwhile, almost no changes occurred in transmittance spectra after illumination on other wavelength (fig 4.3. a, c). It means that optical excitation in the band-gap region is the most efficient, since the photons with necessary energy penetrate the whole volume, exciting electron-hole pairs and further bond-changes. The shorter wavelengths are less efficient because of the high surface absorption, and only the much higher energy particles (electrons in our experiments) are able to generate similar processes.

It is useful to look at the structure of this material to understand the excitation-bond switch processes. The crystalline arsenic-trisulphide (As_2S_3) has a monoclinic structure. Each arsenic atom has five valence electrons and three of them establish strong covalent bonds with sulphur. The other two electrons establish non-bonding s^2 pairs. Two of the six sulphur electrons are bonded with arsenic and four of them are independent nonbonding electrons in s^2 state and two create the so-called lone-pair *lp*-electrons. As a consequence each sulphur atom is surrounded by two atoms of arsenic and each atom of arsenic is surrounded by three atoms of sulphur. The molecular structure of crystalline As_2S_3 is pyramidal. The arsenic atom is situated on the top of the pyramid and the sulphur atoms constitute the bottom which create bonds with neighboring arsenic atoms. Such molecular structure is characterized by Van der Waals interaction. Fast quenching of melted As_2S_3 causes the occurrence of strong covalent bonding between arsenic and sulphur, which poses creations of complex compounds with absence of LRO. In such a way the amorphous state of As_2S_3 with SRO is formed. FTIR and X-ray measurements [98] imply to As_2S_3 as structural elements in the glassy system. Therefore, the physical properties of a non crystalline system differ from the crystalline one according to the preparation conditions and these can be changed by the additional external influences, excitation of non-bonding LP electrons as well as covalent bonds.

These assumptions are supported by the following experiments on the model Se/As_2S_3, where the illumination influences the chalcogen constituent in the spectral region of the absorption edge. In our measurements, Se/As_2S_3 samples with the modulation period of $\Lambda = 8.5$ nm, thicknesses of constituent components $d(As_2S_3) = 4.5$ nm and $d(Se) = 4$ nm were prepared by TVE. The number of bi-layers was set to 100. Thus, the total thickness of the sample is $d_{tot} = 0.84$ μm. Optical transmission

measurements show a sharp absorption edge, which is located in a narrow bandwidth, determined by the smaller E_g of selenium (figure 4.4. curve 1).

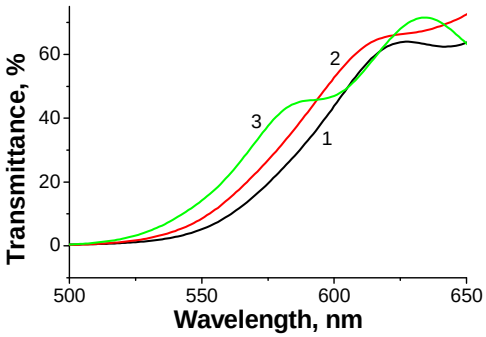

Figure 4.4. Optical transmittance spectra of 1) as deposited, 2) irradiated, 3) annealed Se/As_2S_3

The spectral dependence of photoinduced effect was investigated by millisecond resolution spectrophotometer according to the scheme in figure 3.4. *In situ* irradiation of the sample was preformed by λ = 532 nm wavelength laser light with intensity I = 13 W/cm^2 according to the scheme illustrated in figure 3.4. Since the absorption edge is located near λ = 530 nm it is evident that bleaching kinetic is faster and more prominent near the correspondent wavelength and the change of transmittance behaves unequally at different wavelengths as it can be observed in figure 4.5. Here the absolute and relative transmissions are presented.

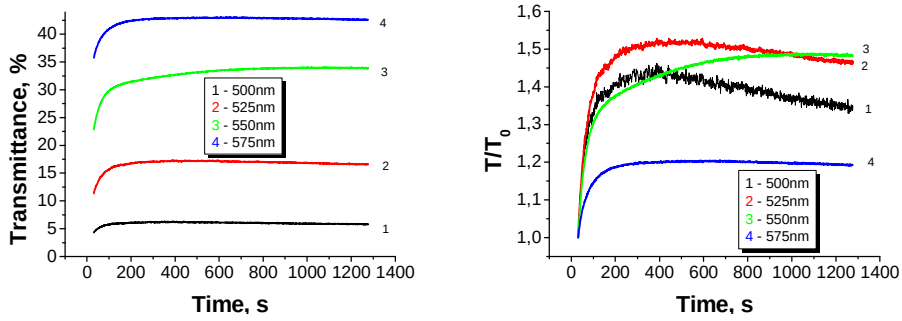

a b

Figure 4.5. The change of absolute (a) and relative (b) transmissions during irradiation of the sample Se/As_2S_3 with λ = 532 nm and I = 13 W/cm^2 laser light.

Photobleaching with consequent short wave shift of the absorption edge was induced also by annealing the sample at 90 °C (fig.4.4. curve 3). Because the magnitude of the photobleaching is more prominent after annealing than after illumination, it is worth mentioning that process still has a heat induced component, although the final result of intermixing is the same. Thus, the heat induced diffusion coefficient calculation is considered more informative in this case. The diffusion coefficient characterizing the interdiffusion of the layered structure was obtained from evaluating the LAXRD spectra kinetics. The logarithm of the relative intensity of the first Bragg-peak decreases linearly with time, and the diffusion coefficient can be obtained by fitting the data according to the formula [99]:

$$\frac{d}{dt}\left[\ln\left(\frac{I}{I_0}\right)\right] = -\frac{8\pi^2}{\Lambda^2} D \ , \qquad (4.1)$$

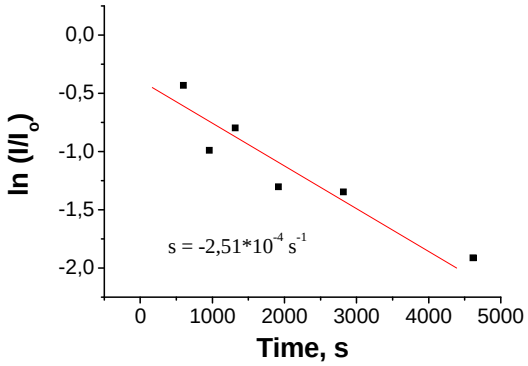

Figure 4.6. Relative Bragg-peak intensity vs. annealing time. Least square fit was applied in the calculation of the diffusion coefficient, the Se/As_2S_3 sample was annealed at 90°C

where Λ is the modulation period of the sample. Denoting the tangent of the fitted slope by *s*, the following working formula was used

$$D = -\frac{\Lambda^2 \cdot s}{8\pi^2} \qquad (4.2)$$

Substituting the value of modulation period and the slope of the points fitting from the figure 4.6 one obtains for the thermal interdiffusion a coefficient $D = 2.29\times10^{-22}$ m^2/s for Se/As_2S_3 structure.

It is a well known fact that chalcogenides of As-Se-S composition show photoexpansion [100]. Se/As_2S_3 NLS also exhibit similar behavior [101]. For investigation of the volume expansion, the samples were irradiated according to the scheme in figure 3.9.

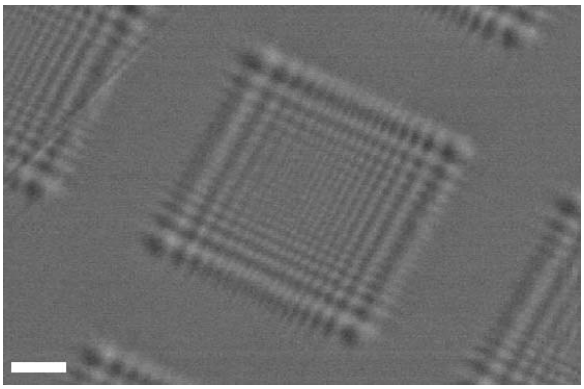

Figure 4.7. SEM picture of the diffraction pattern (bar = 10μm)

The SEM picture of the pattern on the irradiated surface (according to the diffraction on a grid mask) is shown in figure 4.7. A well defined periodic structure is observable. The change of the volume induced by irradiation was investigated by AFM measurements (figure 4.8.). According to the distribution of excitation intensity (diffraction on the grid elements), the first peak is suitable for determination of the maximum of the induced volume change. The AFM measurement indicated as much as 10% of surplus, e.g. the first peak reached about Δd = 85 nm in height while the total thickness of the sample was d = 840 nm. These results correlate well with the observations of other authors [102].

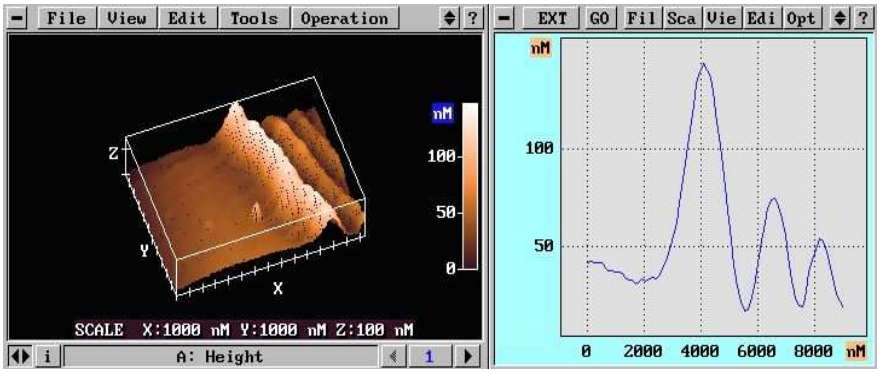

Figure 4.8. Surface view of the illuminated Se/As_2S_3 sample. The AFM scan indicates the possibility of about 10% change in thickness (volume)

Having these results on a model Se/As_2S_3 NML for comparison we moved towards the new structures. Unfortunately, the TVE method is not suitable for preparation of all types of compositions desired to carry on our experiments. These compositions, nevertheless, can be prepared easily by PLD technique. The question relating to structural and chemical properties of samples prepared by the aforementioned methods was answered by comparison of properties of composites which were prepared by both TVE and PLD methods. For this reason reference Se/As_2S_3 multilayered samples were first prepared by PLD and TVE with the same modulation period. The obtained Raman-spectra indicate close similarity of compositions of the samples (figure 4.9.) [103].

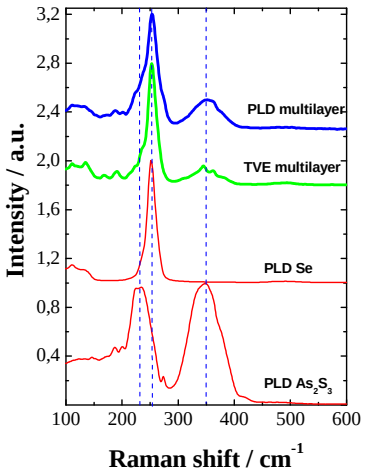

Figure 4.9. Raman-spectra of Se/As_2S_3 samples prepared by PLD and TVE methods as well as of the separate constituent layers.

The appropriate Raman-scattering peaks of PLD and TVE samples are located similarly (figure 4.9. top two curves) and correspond to the constituents Se and As_2S_3 (figure 4.9. bottom two curves). LAXRD measurements indicate sharp interfaces, which vanish during heat treatment, as shown in figure 4.10. The effective annealing temperature of the PLD prepared sample was analogous to the TVE prepared sample.

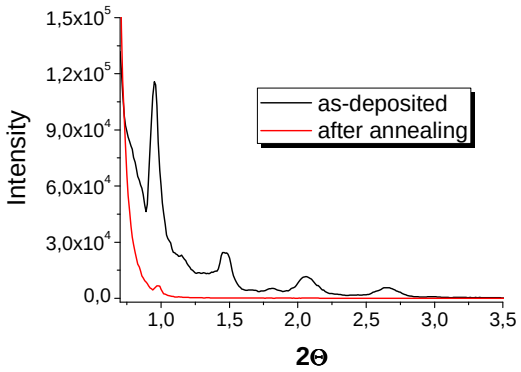

Figure 4.10. LAXRD of as deposited and annealed PLD prepared Se/As_2S_3 sample

It follows from our experiments that the structural, chemical and the related properties of Se/As_2S_3 samples prepared by TVE and PLD methods are similar. The SRO of the thin films does not depend on the preparation conditions. On the other hand, the AFM study of irradiation induced surface diffraction patterns refers to significant increase of the surface roughness of PLD prepared samples [103]. In this respect the sample prepared by TVE is smoother than the PLD prepared one, nevertheless the change of relative volume reaches 10% as well, as can be seen in figure 4.11. These irregularities are most probably connected with the highly non-equilibrium process of pulsed laser deposition. The deposited vapour consists of a big amount of clusters and nanosized fragments of the evaporated target, which support the conservation of the average composition but introduce additional structural irregularities due to the fast condensation and lack of local diffusion to the more equilibrium state of the layer.

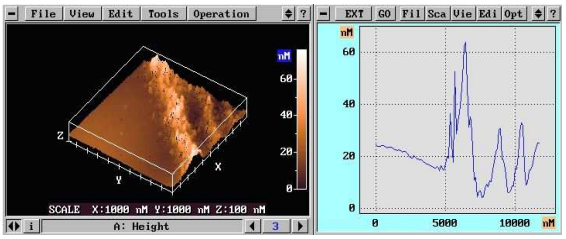

Figure 4.11. Surface view of the illuminated PLD prepared Se/As_2S_3 sample. The AFM scan indicates the possibility of 10% thickness change.

As a general result, we assumed that chalcogenide NML samples prepared by two different techniques behave similarly, e.g. their main structural and chemical changes and the interdiffusion act similarly. It is supported also by the fact that the calculated diffusion coefficient for thermally induced interdiffusion in PLD prepared sample correlates well with TVE prepared ones (D_{PLD} = 2.23×10^{-22} m^2/s, D_{TVE} = 2.29×10^{-22} m^2/s) [103]. These facts open new possibilities in fabrication of nanolayered samples. Samples which are not suitable for TVE preparation can be prepared by PLD. A composition like GeSe/GeS is hard to prepare by TVE because of the difference in vaporization pressure of the constituent alloys.

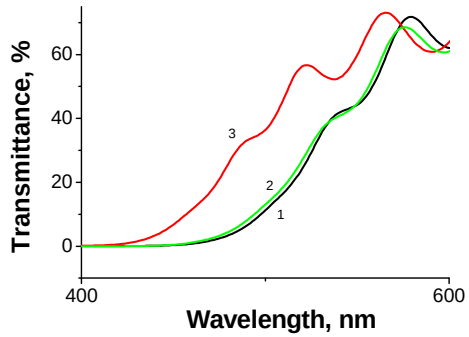

Figure 4.12. Transmittance spectra of 1) as deposited, 2) irradiated, 3) annealed GeSe/GeS

For this purpose the PLD preparation technique is more suitable, the stochiometry of the evaporated material retains the target one. A similar conclusion on the PLD technology was made by other authors [6].

Optical transmittance spectra of PLD prepared GeSe/GeS are shown in figure 4.12. The spectrum is characterized by a sharp absorption edge and it shifts after annealing or illumination. Cross-sections of the transmittance spectra are presented on figure 4.13, obtained according to the *in situ* illumination scheme (see figure 3.4). The relative units and absolute transmittance values are shown as a function of duration of light action.

It is seen from the transmittance spectrum (figure 4.12.) that the green laser light, whose wavelength is close to the absorption edge (estimated from $(\alpha h\nu)^{1/2}$ Tauc plots, E_g = 2.07 ± 0.01 eV), is suitable to induce a shift of the absorption edge due to the intermixing of the components. Therefore *in situ* illumination was induced by λ = 532 nm wavelength laser light with the intensity I = 13 W/cm^2.

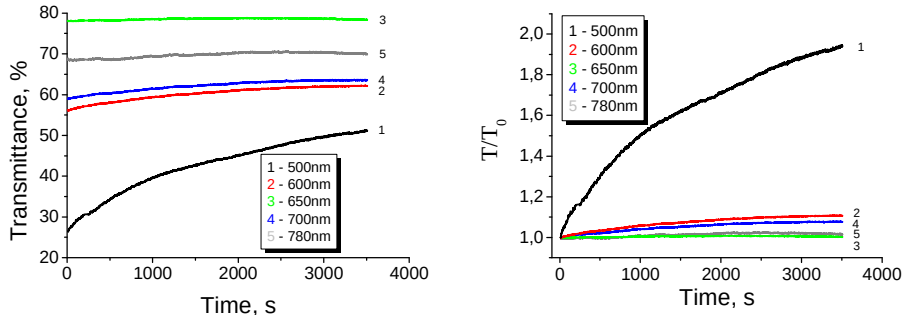

a b

Figure 4.13. The change of absolute (a) and relative (b) transmissions during illumination of GeSe/GeS

The bleaching kinetics indicate a well pronounced dependence on the wavelength of the irradiation (figure 4.13. a). While the relative bleaching yields T/T_0 = 2 on λ = 500 nm, it hardly reaches the value of 1.1-1.2 on other wavelengths. It seems evident to connect this dependence with differences in the absorption coefficient, i.e. in the efficiency of the excitation of the chalcogenide sub-layers, which are first of all responsible for the stimulated interdiffusion.

Concerning the contribution of annealing to the structural change, the similar shift of the absorption edge should be pointed out. It can be seen from the figure 4.12 (curve 3) that the resulting shift caused by annealing is more pronounced than that caused by illumination. It is caused by interdiffusion between contacting layers. Relative variation of the LAXRD peak intensity is shown in Fig. 4.14. Diffusion coefficients were estimated using Eq. (4.2): D = 2.12×10^{-22} m^2/s [104].

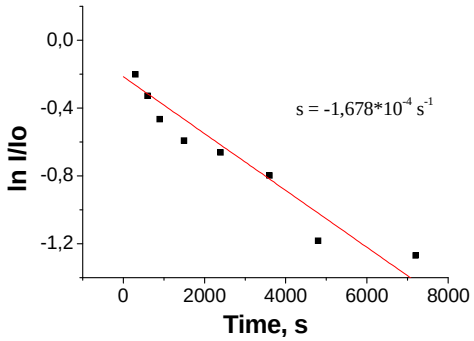

Figure 4.14. Relative Bragg-peak intensity vs. annealing time. Least square fit was applied in the calculation of the diffusion coefficient, GeSe/GeS sample annealed at 225°C

The volume change has been probed with the diffraction pattern writing procedure according to the scheme in figure 3.9. The AFM scan of the irradiated surface is shown in figure 4.15. Peaks of the periodic surface structure correspond to the maximum intensities of the incidental diffraction pattern. The relative magnitude of the induced volume change reaches 8% (total thickness of the samples was 1 μm). The surface roughness is noticeably worse in comparison with the roughness of TVE prepared samples, similar to what it was in the case of Se/As_2S_3 samples.

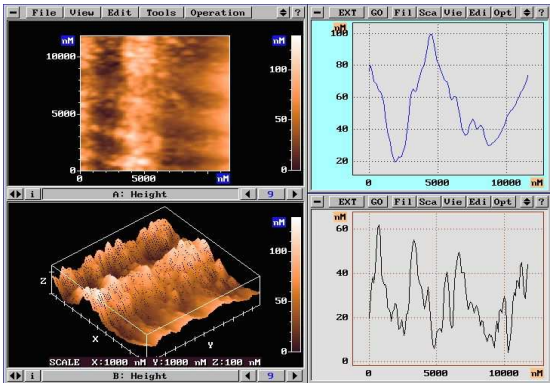

Figure 4.15. AFM surface scan of the laser light illuminated GeSe/GeS sample

This difference in surface quality is well reflected in values of root-mean-square (RMS) of the surface roughness, which for TVE prepared Se/As_2S_3, PLD prepared Se/As_2S_3 and PLD prepared GeSe/GeS samples are 0.91 nm, 1.22 nm and 2.28 nm, respectively [105]. This difference in the surface roughness is connected with the PLD preparation technique. During pulses clusters and bigger fragments are deposited onto the substratum. Nevertheless, optical measurements indicate that it does not influence the optical properties of the sample, being illuminated with much longer wavelengths.

The next type of metal/chalcogenide nanolayered structures studied was Sb/As_2S_3. A nanolayered sample with modulation period of Λ = 6.5 nm, with d(As_2S_3) = 3.15 nm and d(Sb) = 2.45 nm sublayer thicknesses, with the total number of bilayers N = 100 (i.e. the total thickness d = 0.65 μm) was prepared by TVE method. The obtained optical transmittance spectra are presented in figure 4.20.

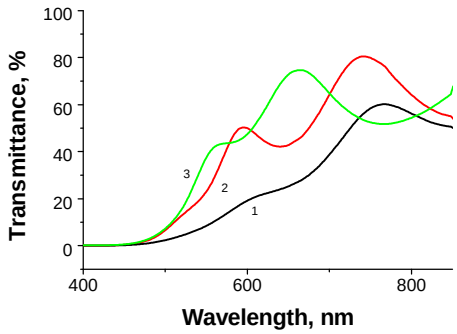

Figure 4.20. Comparison of the transmittance spectra of 1) as deposited, 2) irradiated, 3) annealed Sb/As_2S_3 multilayer

Both the irradiation and annealing cause photobleaching, i.e. the shift of the absorption edge to the shorter wavelength region (curves 2 and 3 in figure 4.20.). Both irradiation and annealing caused shifts of the absorption edge are nearly of the same magnitude. According to our preliminary investigations, it was expected that the sensitivity of samples would not vary significantly around the 550 nm wavelength. The millisecond resolution transmission spectra were gathered during in situ irradiation (scheme in figure 3.4) by green laser light of λ = 532 nm wavelength and intensity I = 13 W/cm^2.

Variation of the optical transmission with time of illumination and the bleaching kinetics are presented in figure 4.21. (a) and (b), respectively.

It can be seen from figure 4.21. (b), that the response to wavelengths λ = 550 nm and λ = 600 nm is equal within the instrumental resolution. Almost the same value was observed at 532 nm. This confirms the assumption regarding the high sensitivity in this wavelength region. According to the absorption edge width location both wavelengths are suitable to induce the highest optical changes. It is noticeable that the magnitude of the absorption edge shift induced by light or heat (figure 4.20. spectra 2 and 3) is similar in contrast to previous mentioned samples of Se or Ge constituents. Therefore, we performed a more detailed investigation in order to compare heat and light induced bleaching behaviors to understand the background of annealing and illumination kinetics.

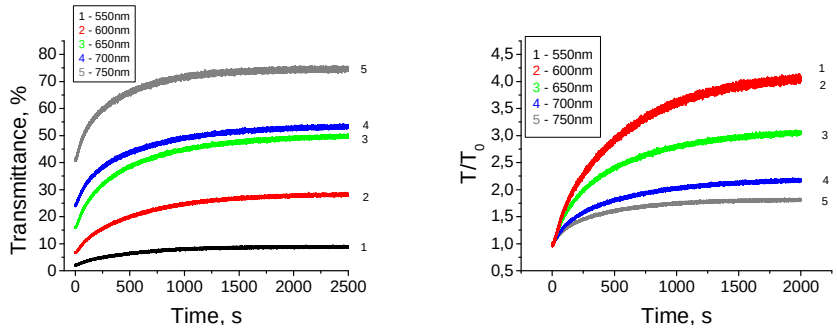

a b

Figure 4.21. The change of absolute (a) and relative (b) transmissions during illumination of Sb/As_2S_3 sample

In situ annealing kinetics was measured at a fixed wavelength corresponding to the green laser light and on three different constant temperatures (T = 90, 100, 110 °C) by Shimadzu spectrophotometer. The obtained results of bleaching kinetics of Sb/As_2S_3 sample shows that thermally and light induced changes behave similarly under certain circumstances.

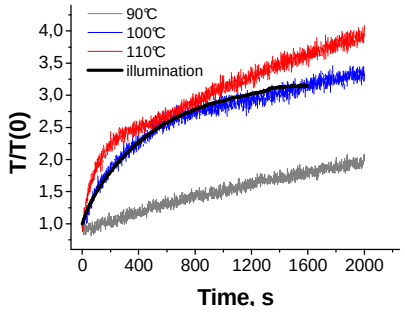

Figure 4.22. Annealing bleaching kinetics of Sb/As_2S_3 at elevated temperatures in comparison with the bleaching under illumination by green laser light (λ=523 nm) at 25°C.

As shown on the figure 4.22., the annealing of the sample at 100°C induces bleaching kinetic which is similar to illumination induced bleaching kinetic at 25°C. It is worth noting that the illumination contributes to local thermal heating as the sample absorbs a certain amount of incident light (figure 4.20.). However, it usually doesn't exceed several degrees in chalcogenide-chalcogenide NMLs, illuminated in the optical band gap range at transmission coefficients near 30% [106]. Taking into account the above-mentioned arguments, the progression of heating and illumination induced processes is assumed to be similar in these samples. At the same time in the case of Sb/As_2S_3 samples they can be investigated independently.

The evaluation of photoinduced intermixing of the constituent layers as well as heat or photon induced diffusion was made from the data of LAXRD spectra. Diffusion coefficients calculated from the time dependence of the first Bragg peak are presented in figure 4.23 for light induced and heat induced interdiffusion.

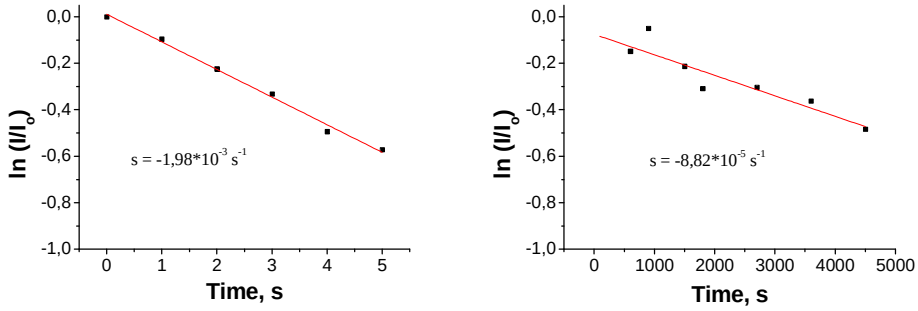

a b

Figure 4.23. Relative Bragg-peak intensity vs. time. Red line is the least square fit for calculations of diffusion coefficients for photo (a) and thermally (b) induced diffusion in Sb/As_2S_3 sample

For the light induced interdiffusion the obtained diffusion coefficient is $D_{light} = 1{,}06\times10^{-21}$ m^2/s, while for the heat induced one $D_{annealing} = 4{,}7\times10^{-23}$ m^2/s. Thus, the rates of the intermixing processes are different, revealing the certain role of non-photon assisted structural changes.

Estimates of photo-induced and thermal diffusion coefficients can be made also using data on optical transmission (Fig. 4.22). It is clear that the increase of the optical transmission at initial stages of intermixing occurs mainly due to dissolution of Sb layers in As_2S_3. Due to the dissolution, the thicknesses of Sb layers decreases with time and thus transmission grows. Computer simulation of this process in the assumption that Sb diffusion coefficient does not depend on the concentration. Fig. 4.24 shows successive stages of dissolution and thinning of the Sb layer.

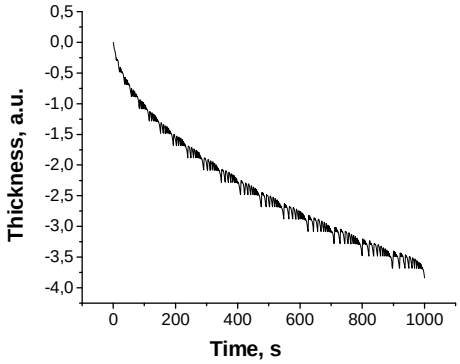

Figure 4.24. Simulation of Sb dissolution in As_2S_3 under illumination

The calculations show that the thickness of each Sb layer decreases with time according to the formula

$$d_{Sb}(t) = d_{Sb}(0) - A(Dt)^{1/2}, \qquad (4.3)$$

where A is a dimensionless coefficient, which depends on the relative thicknesses of the Sb and As_2S_3 layers. As the transmission of the Sb layer varies with its thickness according Eq. (4.3), one can easily find how transmission varies with time:

$$T(t) = (1-R)^2 e^{-\alpha d_{Sb}(t)} = T(0)e^{\alpha A(Dt)^{1/2}} \qquad (4.4)$$

where R and α are the reflection and absorption coefficients, respectively. We neglect variation of R with the layer thickness. As it follows from Eq. (4.4),

$$\ln\frac{T(t)}{T(0)} = \alpha A(Dt)^{1/2} \qquad (4.5)$$

i.e. $\ln[T(t)/T(0)]$ should increase proportionally $t^{1/2}$.

As the absorption coefficient α is known, diffusion coefficient D can be calculated as

$$D = \left\{\frac{1}{\alpha A}\frac{\Delta\ln[T(t)/T(0)]}{\Delta t^{1/2}}\right\}^2 \qquad (4.6)$$

In Fig.4.25 we present dependences $\ln[T(t)/T(0)]$ versus $t^{1/2}$ both for thermal and photo-induced diffusion. Some deviation from linear dependence can be attributed to possible dependence of reflectivity R on the thickness of Sb layer because of the appearance of discontinuousity of Sb layer during dissolution. This can be a reason for differences between LAXRD and optical methods: we have estimated diffusion coefficient using tangent at t = 0 and obtained for thermal diffusion: $D_{annealing} = 1{,}0\times10^{-20}$ m^2/s at 100 ^oC , and for photo-induced diffusion $D_{light} = 1{,}2\times10^{-18}$ m^2/s at room temperature taking thickness parameter A in formulae (4.6) as 1. It means that the action of light is similar to thermally activated diffusion with regards to the structural changes in NML, but the mechanism is connected with non-equilibrium process of excitation by light (or e-beam, as it will be shown later).

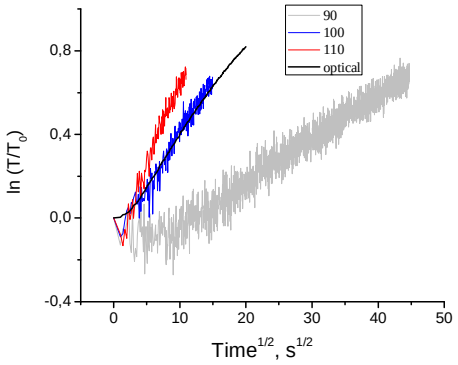

Figure 4.25. Relative transmittance change during annealing and illumination

Noticeable light induced volume change was not observed even by AFM investigations in these samples. At the same time the Sb/As_2S_3 sample exhibited the largest refraction index change compared with other samples. While the change of refraction index reaches Δn = 0.1 for GeSe/GeS, Bi/As_2S_3 [106-107] and Se/As_2S_3 samples, the change of refraction index for Sb/As_2S_3 reaches Δn = 0.3 (see figures 4.26, 4.27).

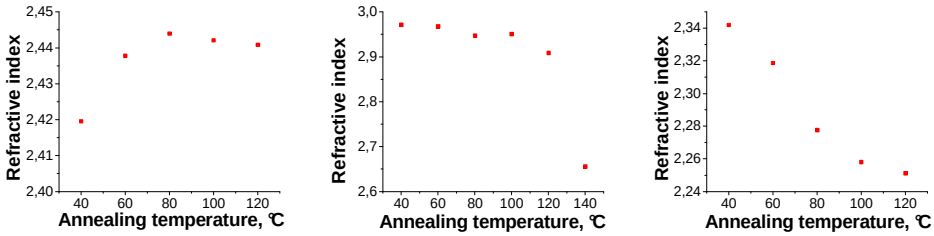

a) b) c)

Figure 4.26. The change of refractive index during annealing of a) Se/As_2S_3, b) Sb/As_2S_3 and c) GeSe/GeS samples

The behavior of the dependences of *n* on annealing temperature and illumination is different for the selected examples of NML, which is connected with the appropriate change of the refractive index in the proper binary or ternary systems [2]: in Se-As_2S_3 it increases due to the introduction of Se to the As_2S_3 matrix, but in the case of Sb(Bi)/As_2S_3 or GeS/GeSe NMLs the effective *n* of the nanomultilayer is larger than

the refractive index of the mixture, obtained here as a consequence of solid phase synthesis.

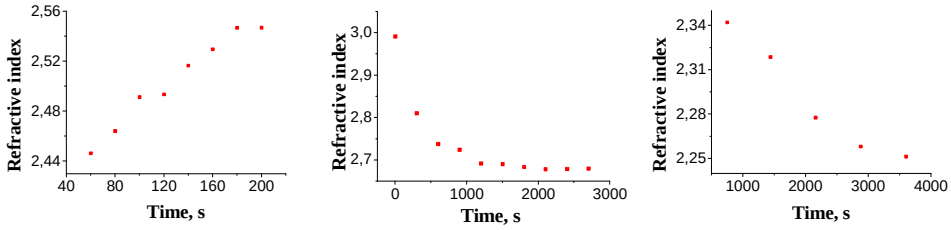

a) b) c)

Figure 4.27. Change of the refractive index during illumination of a) Se/As_2S_3, b) Sb/As_2S_3 and c) GeSe/GeS samples

It is worth mentioning that the nanolayered samples with In or Au constituent (Au/As_2S_3, In/As_2S_3) exhibit no volume change as well [108]. We concluded from our experiments that all nanolayered samples with metals or semi-metals content do not exhibit volume change during illumination at all. This is an important basic result and it can find certain application also in recording systems, where volume changes are not desirable. Therefore, in the next part of our work we focused on investigations to define and describe the chemical and structural changes which occur in metal-containing nanolayered chalcogenides during illumination.

An XPS measurement of investigated samples gives additional information about the chemical state of the matter. Se/As_2S_3 nanolayered samples have been investigated and described in detail by Adarsh at.al. [109]. By probing the electronic structure of the top layers, the chemical interaction between As_2S_3 and Sb layers can be analyzed. We have determined the chemical composition of the Sb/As_2S_3 multilayer sandwich structure with Sb film at the top. Using the areas under XPS core level peaks, the result is S:Sb:As = 51:28:21 in at.%. Taking into account the 1 nm thickness of the top Sb layer and that 65% of the signal originates from the first 3 nm of the surface, one can conclude that the observed significant decrease in As/S ratio of As_2S_3 from 0.67 to 0.41 would be impossible without the partial interdiffusion of Sb and As_2S_3 layers at the deposition stage and/or due to the exposure to X-rays. The existence of partial

interdiffusion is backed by the fact that the composition of a single As_2S_3 layer did not differ significantly from the bulk glass used for the film deposition.

The core level spectra for metallic Sb and glassy As_2S_3 thin films are considered as references. The comparison of Sb $3d_{3/2}$ spectra of the freshly deposited metallic Sb and Sb/As_2S_3 multilayers (fig. 4.28.) confirms the formation of new Sb-containing compound in the latter.

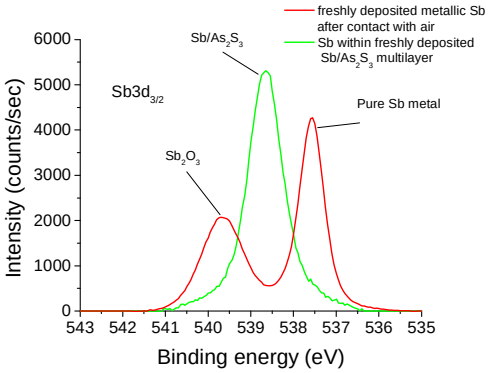

Figure 4.28. Sb $3d_{3/2}$ spectra of the freshly deposited metallic Sb and Sb/As_2S_3 sample

Position of the peak associated with the new compound is between pure Sb [110] and Sb_2O_3 [111]. According to the reference [112], the binding energy of this compound is close to that reported for Sb_2S_3. The same conclusions can be made by comparing Sb 4d spectra. The Sb $3d_{5/2}$ component can not be reliably used because of its overlap with O 1s spectrum. The difference in electronegativity of As and Sb atoms (2.18 and 2.05 [113] is the main reason for the observed 1.2 eV chemical shift of the S 2p peak for As_2S_3 film vs. Sb/As_2S_3 multilayer sandwich (fig. 4.29.).

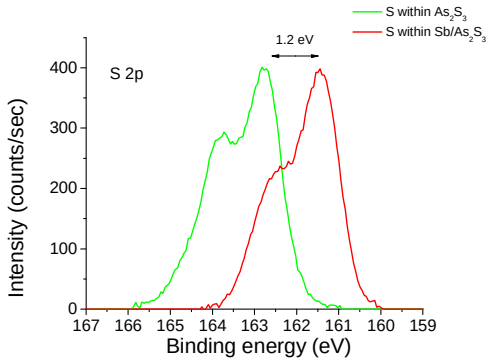

Figure 4.29. S 2p peak for As_2S_3 and Sb/As_2S_3 sample

It means that the $As_2S_3 \rightarrow Sb_2S_3$ is the main structural transformation during interdiffusion between the adjacent layers. The same transformation can be seen also from the analysis of As 3d spectra (fig. 4.30.), where a 1.0 eV chemical shift is linked with the formation of As-As homopolar bonds in place of heteropolar As-S bonds.

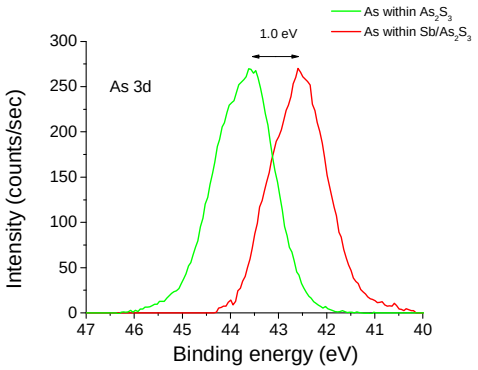

Figure 4.30. As 3d spectra for As_2S_3 and Sb/As_2S_3 sample

The fitting of the Sb 3d core level peak (fig. 4.31.) of the freshly prepared multilayer suggests that ~10-15 at.% of Sb atoms form oxide, most probably Sb_2O_3. This is represented by components marked '2' at 539.7 eV (for Sb $3d_{3/2}$) and 530.0 eV (for Sb $3d_{5/2}$), which coincides with the oxide observed on metallic Sb (fig. 4.28). Most of the Sb atoms are organized in $SbS_{3/2}$ pyramids (component 1, fig. 4.31), but ~10 at.% of all Sb atoms still exists, most probably within the Sb-Sb homopolar bonds

(component 3, fig. 4.31.). The wide oxygen 1s component (FWHM higher than 1.7 eV) at 531.8 eV belongs most likely to both adventitious hydroxide groups and the oxygen bonded with Sb. The shape and positions of As 3d peak exclude As oxidation in this sample.

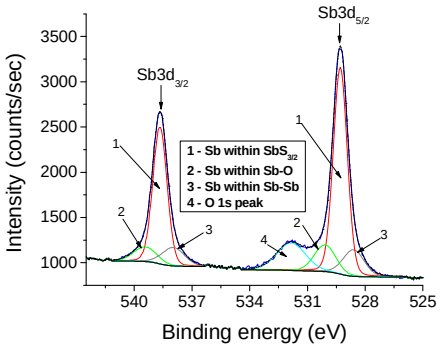

Figure 4.31. Sb peaks of freshly deposited samples

The above described chemical environment of Sb in a freshly deposited Sb/As_2S_3 multilayer is confirmed also by the fitting of Sb 4d core level spectrum (fig. 4.32.). The binding energies of the Sb 4d components are close to those reported for $Ge_{23.5}Sb_{11.8}S_{64.7}$ using 284.8 eV C1s line as the reference [114].

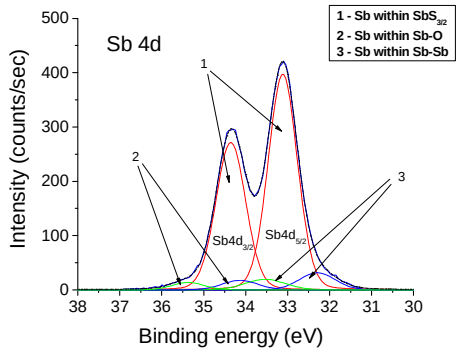

Figure 4.32. Sb peaks of freshly deposited sample

Fitting of S2p XPS core level spectrum of non-irradiated multilayer sample shows two distinct pairs of spin-orbit split components (fig. 4.33.). The major component (1 in figure 4.32; ~72 % of S atoms) at lower binding energy (161.4 eV for $S2p_{3/2}$) can be associated with 2-fold coordinated S linked with the lower

electronegativity Sb within the $SbS_{3/2}$ pyramids [115]. The results show that there are no more $AsS_{3/2}$ pyramids (observed at 162.5 eV for $S2p_{3/2}$, fig. 4.29.) left in the structure after interdiffusion. It suggests that the minor component at 161.9 eV belongs to Sb-S-As fragments. S atoms in these fragments are characterized by the value of XPS binding energy between the values for $AsS_{3/2}$ and $SbS_{3/2}$. According to my best knowledge this conclusion can be regarded as the first result in the literature on high resolution XPS study of thin films in this glassy ternary system.

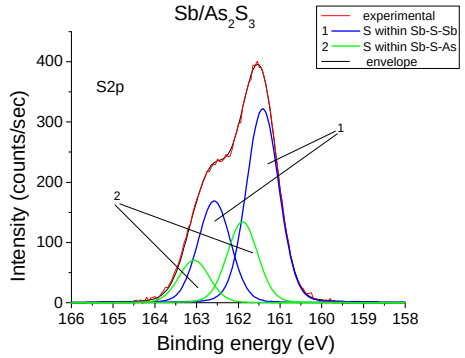

Figure 4.33. S2p spectrum for freshly deposited sample

The analysis of As3d spectrum for the freshly prepared multilayer is not unique because of numerous fitting possibilities. The position of these spectra and the above fitting of the S2p spectrum allow us to conclude that the majority of As atoms form homopolar As-As bond within 3-fold coordinated and some other complex units. A fraction of As atoms is still within As-S bonds without the formation $AsS_{3/2}$ pyramids. Also, the very top of the sandwich is covered by Sb oxide; it appears to prevent the oxidation of arsenic.

Laser irradiation significantly enhances oxidation of both As and Sb (fig. 4.34. and fig. 4.35). The concentration ratio of the main elements is S: 32%, As: 24% and Sb: 44%. Due to oxidation, the As/S ratio in the analyzed surface region of the sandwich drastically increases from 0.34 to 0.75, the top ~10 nm layer becomes strongly As-rich or S-depleted. Those Sb atoms which are not bonded to oxygen form $SbS_{3/2}$ pyramids. Analysis of S2p XPS peak shows that the concentration of S atoms within As-S bonds decreases to less than 10 % of all S atoms. Except for those present in arsenic oxide, the

arsenic atoms are mostly in the units containing both As-As and As-S bonds or in As clusters.

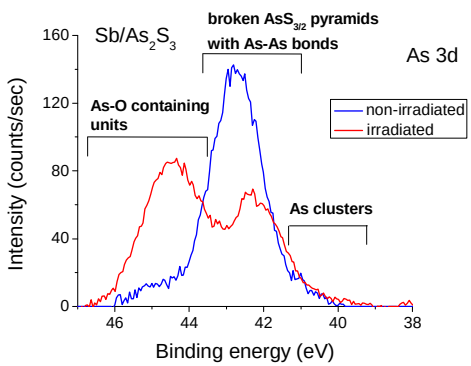

Figure 4.34. As peaks

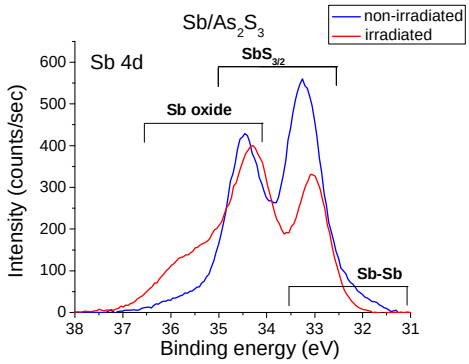

Figure 4.35. Sb peaks

It is reasonable to assume that a strong oxidation effect takes place only at the surface of the NLS during thermal or light-induced interdiffusion which can also influence the structure of the matrix: possibly it can be broken to small clusters or islands of different composition. Nevertheless the interdiffusion process in the interior leads to essential changes of optical parameters. At the same time, contrary to the case of Se/As_2S_3 NLS, no volume increase or local expansion was observed during AFM surface profiling of lines or gratings previously recorded in the investigated Sb/As_2S_3 nanolayered structures. This difference can be explained at least by three causes of the photoinduced volume change in Se/As_2S_3 which are absent or less probable in Sb/As_2S_3. In Se/As_2S_3 all these causes may be connected with the creation of chalcogen-related “wrong bonds” and defects like -S-Se- and three-fold coordinated chalcogen in -As-S-As-S-As- chains during interdiffusion under illumination, which makes possible: a) the appearance of Coulomb repulsive forces between the charged structural units [116, 117] and the local expansion of the photo-softened [118] material, b) the increase of disorder and free volume in the chalcogenide glass due to the increased number of defect bonds related to the chalcogen atoms [119, 120], and the related c) decrease of the density of As-S-Se solid solution in comparison with one calculated for the composite [121]. The introduction of Sb atoms causes passivation of

above mentioned defects, since according to our above analyzed results Sb actively creates bonds with chalcogen atoms. The oxidation processes can also inhibit the volume change.

For more detailed understanding the exact interdiffusion process, low temperature *in situ* transmittance kinetics was compared with room temperature transmittance kinetics for Se/As_2S_3, Sb/As_2S_3 and In/As_2S_3 nanolayered chalcogenides (fig. 4.36. a, b and c). The samples were placed in a vacuum cryo chamber, which was equipped with two optically transparent viewport windows. The sample temperature was stabilized at 100 K using liquid nitrogen cooling. Green laser light with $\lambda = 523$ nm wavelength was applied for sample illumination which at the same time served as reference light source. Thus, the change of relative transmissions was determined. In all cases the samples showed photobleaching effect. Attributing these changes to intermixing, one can assert that we have detected photo-induced diffusion at 100 K. It is worth noting, however, that the bleaching kinetics at low temperatures has a non exponential character [122].

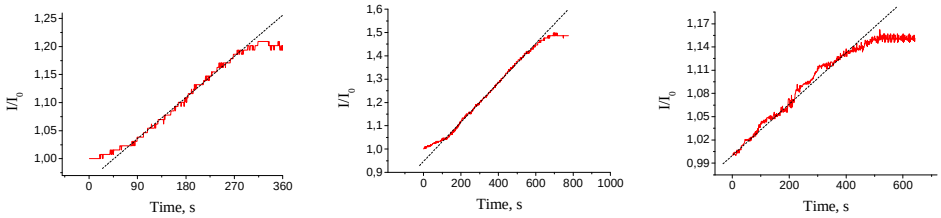

Figure 4.36. Bleaching kinetics during illumination of Se/As_2S_3 (a), In/As_2S_3 (b) and Sb/As_2S_3 (c) at low temperature.

Such low temperature behaviors can be explained by an intermixing effect, which does not follow Fick's law. An important support to this assumption is given by the measurements of photo-stimulated changes of the transmission spectra at liquid helium temperatures (see figure 4.37.). Samples were measured with respect to the observed optical transmission changes (bleaching at certain wavelengths) in an acceptable time domain under the influence of green ($\lambda = 530$ nm, L1 in Fig.4.24.) or red ($\lambda = 630$ nm,

L2 in Fig.4.37.) laser irradiation with power densities between 0.1-10 W/cm^2. Optical transmission measurements at room and low (4.2-100 K) temperatures were performed.

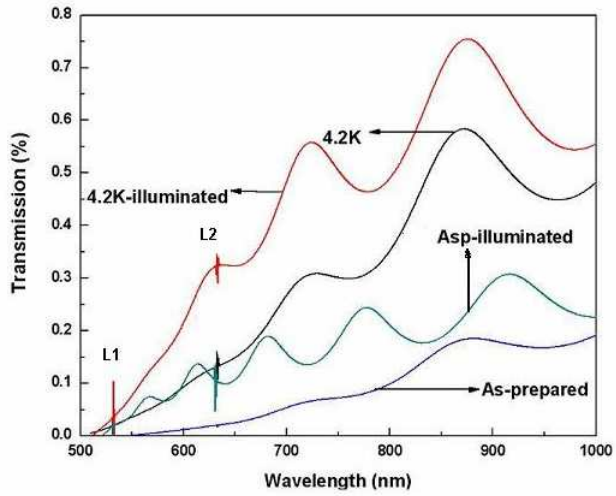

Figure 4.37. Transmission spectra of Sb/As_2S_3 film at room temperature and 4.2K, before (as prepared) and after the illumination.

The laser light is able to excite or break bonds as the binding energy does not change with temperature. Therefore, atomic displacements and fluctuations in atomic interactions occur as well. As a result, the spatial distribution of atoms changes in time, which causes an atomic intermixing. At low enough temperatures vacancy creation differs from a room temperature one as vacancies are “frozen” and cannot migrate in the matter. Therefore viscosity appears to be high, vacancies are localized and their migration is limited. In such manner the linear behaviors (instead of exponential following from the Fick’s law) are predictable, what is obtained.

It can be concluded that one of two components of diffusion (the light induced one) behaves like a ballistic transport and does not change due to the cooling, except for the influence of excitation cross sections and lifetimes of defects at low temperatures, while the thermally induced one disappears at low temperatures. This assumption follows also from the novel model of photo-induced mass-transport in amorphous chalcogenides [123].

The advantage of induced interdiffusion of a more- and a less-absorptive layer of a nanolayered chalcogenide-based composite consists in the creation of solid solutions with a changed optical absorption edge. Irradiation by laser light with wavelength corresponding to the optical band gap of the matrix material induces interdiffusion, where the light penetrates all sub-layers and the absorption is still rather efficient. Laser exposure leads to solid state synthesis of a three-component material from initially separated nano-layers. We note that heating from laser irradiation can not be the primary cause of the observed photo-bleaching, since a similar effect was observed at low temperature (fig. 4.36.) measurements, too.

Thesis based on corresponding chapter

1. I have established by experiments that the thermal vacuum evaporation and the pulsed laser deposition methods are equally suitable for fabrication of nanolayered amorphous chalcogenides. It was demonstrated by Raman-spectroscopy measurements that the Se/As_2S_3, $Ge_{20}Se_{80}/Ge_{33}S_{67}$ samples which were prepared by these two methods had the same structural characteristics. By supplementary photo-spectroscopic measurements I have shown similar photoinduced changes (shift of the optical absorption edge and increase of optical transmission) in both types of samples. The differences in the morphology and surface roughness of these samples, which were measured by atomic force microscope, are caused by the circumstances of the deposition.

2. According to my investigations, layered structures which contain metals or semimetals (Bi, Sb, In, Au) do not exhibit photo-induced volume change, contrary to the well known amorphous chalcogenide layers ($As_{20}Se_{80}$, As_2S_3) or amorphous multilayers made of these materials. On the other hand, the changes in optical parameters have the same character in multilayers: the transparency increases, the absorption edge shifts to the shorter wavelength range, and the refractive index changes. At the same time, the low angle X-ray diffraction measurements show that the neighboring layers are mixing.

4.2. Electron-beam induced surface patterning

As previously mentioned, chalcogenide glasses exhibit a number of structural changes when exposed to electron beam [124-125]. Shift of the absorption edge or surface deformation have been observed in bulk and thin films under electron beam exposition. Expositions were made onto sample surfaces without any conducting covering, on the one hand, and, in order to acquire good quality patterns, with a gold layer surface coating to perform charging effects free surfaces, on the other.

The basic lithographic process is an essential part of nearly all planar patterning processes. High resolution lithography is an important technological pursuit in research and development because it enables both high performance and unique device applications, and because of its economic importance in industry.

Experimental setup, as described in Chapter 3, in general consists of SEM equipped with a beam-blanker. Total exposure time can be denoted as:

$$T = \frac{QA}{I} \qquad (5.1)$$

I – the beam current delivered to the workpiece

A – the area on the wafer to be exposed

Q – the charge density to be delivered to the exposed region (often called like “dose”)

The beam current is related to the beam half-angle (α) and the diameter of the spot focused on the substrate (d) by the relationship:

$$I = \beta\left(\frac{\pi d^2}{4}\right)\left(\pi\alpha^2\right) \qquad (5.2)$$

β – is the brightness of the source.

In general the current density in the spot is not uniform, but rather consists of a bell-shaped distribution. As a result, d corresponds to an effective spot diameter.

Thomson-Whiddington law gives the energy loss of the electron beam when it passes through the amorphous resist [126]:

$$E_A^2 - E_B^2 = b'z \qquad (5.3)$$

$$b' = 6{,}9\times 10^9 \left(\frac{\rho E_A^{0,5}}{Z^{0,2}} \right) \qquad (5.4)$$

E_A – energy of the electrons when they enter the resist (in eV)

E_B – energy of the electrons when they exit (in eV)

z – thickness of the resist (in cm)

ρ – density of the resist (in g/cm^3)

Z – effective atomic number

Since sample constituents mainly consist of chalcogenides, which are semiconductors and inorganic photoresists, we can write the power dissipated in nanolayered samples as:

$$P_k = I_k \Delta E_f , \quad (5.5)$$

where I is the current of electron beam, and $\Delta E_f = E_A - E_B$.

Bishop's data [127] indicate that the mean energy of the backscattered electrons is 60% of the incident energy. If the mean electron energy is known as the electrons enter the resist, one cannot use the Thomson-Whiddington law to calculate the energy lost in the resist film, ΔE_B, for two reasons: first, the spread of electrons is wide and, second, the directions of travel of the backscattered electrons are not normal to the resist substrate interface, in general.

The quantity that controls the change in solubility of a resist is the total energy absorbed per unit volume (energy density), ε (J·m^{-3}). Assuming that the energy is uniformly absorbed in a resist layer of thickness z, ε is related to the exposure dose Q by the expression

$$\varepsilon = \frac{\Delta E_f \left(1+\eta_e\right)}{z} Q \qquad (5.6)$$

For example, this equation indicates that an exposure dose of 1μC·cm^{-2} corresponds to an absorbed energy density of 3,6·10^{7} J·m^{-3}

Deviation for spatial distribution of energy may be expressed as σ_f (in μm)

$$\sigma_f = \left(\frac{9{,}46z}{V}\right)^{1{,}75} \qquad (5.7)$$

V – accelerating voltage in keV

z – thickness in μm,

which in this case of investigated samples σ = 0,25 μm.

In the first step a pilot Se/AsS sample was irradiated by electron beam. Pressure in the sample chamber was 10^{-3} mPa, accelerating voltage was 10 kV, aperture size 200μm and the working distance 20 mm.

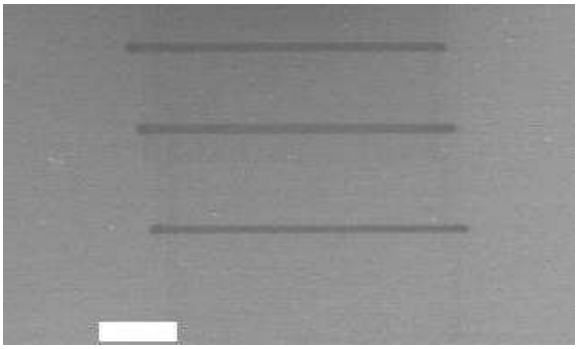

Figure 4.35. Irradiation imprints after scanning in SEM (the bar = 1 μm). Lines were irradiated with dose Q = 0.5 C/cm^2 (bottom), Q = 1 C/cm^2 (middle) and Q = 1.5 (top) C/cm^2

Three lines on the sample surface were irradiated in a SEM microscope in a dot-by-dot manner by the e-beam. The irradiation current was measured beforehand by a Faraday cup. Thus, the dose was determined as a function of the scanning time. The obtained three irradiated lines with 0.5, 1 and 1.5 C/cm^2 doses are presented in the figure 4.35.

AFM investigation of the irradiated surface (see fig. 4.36.) reveals significant change in the volume of several percents that correlates with data of Tanaka [128].

The pilot GeSe/GeS and Sb/As_2S_3 samples were irradiated under the same conditions. After systematic measurements GeSe/GeS samples showed similar behaviors with the same irradiation doses, while Sb/As_2S_3 samples did not exhibit any surface change even at higher doses.

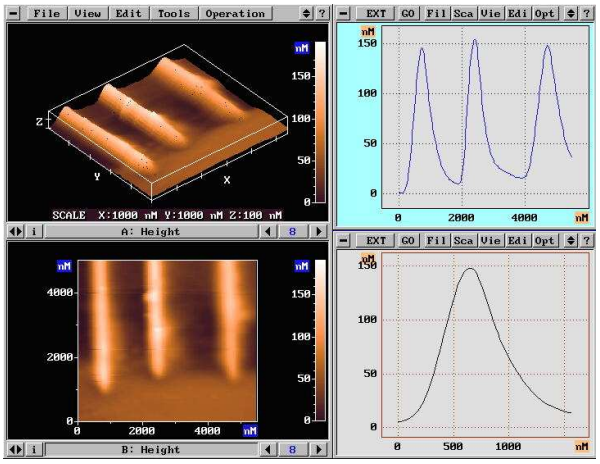

Figure 4.36. Imprints of the e-beam irradiation on the Se/AsS sample

Detailed investigations of the e-beam irradiation caused surface changes were investigated by LEO 1550 VP FE-SEM e-beam lithography system. Experimental setup is presented schematically in figure 3.6. Irradiation of conducting coating free as-deposited samples was made at 30 Pa pressure in nitrogen environment. The accelerating voltage during writing process varied between 5 to 30 kV. The beam current was measured by a Faraday-cup before each run. In order to minimize the scattering of electrons on nitrogen atoms, working distance during patterning was kept constant at 3 mm. Finally, beam spot was focused onto a spot approximately 1 nm in diameter.

In order to find the optimum conditions and dose for the electron-beam irradiation, a matrix of 64 empty 5 μm × 5 μm squares with 5 μm spacing between them was recorded on the surface of the sample. In this way a matrix of 8 × 8 separate structures, each one with a different dose, was formed. Accelerating voltage was

determined by systematic measurements and a Monte-Carlo simulation using CASINO V2.42 software [129]. In these calculations the accelerating voltage was chosen to 30 kV for penetration into Sb/As_2S_3 and Se/As_2S_3 NLS, although already the 15 kV acceleration voltage ensures more than 80 % of the total electron energy to be absorbed in both structures (fig. 4.37.) [130, 131].

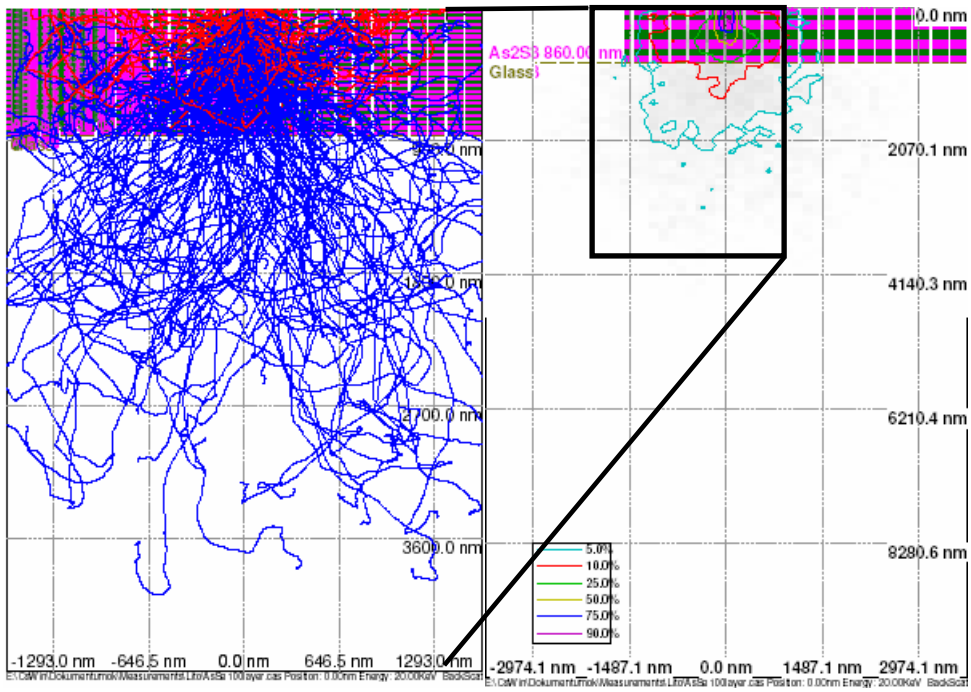

(a) (b)

Figure 4.37. Electron scattering trajectories (a) and energy distribution (b) in a nanolayered sample. The calculation was made by Monte-Carlo simulation [130]. Acceleration voltage was 15 kV.

The beam current was kept constant. The dose variation was realized through the variation of the irradiation time, which was calculated and set by the guiding software.

Three types of nanolayered samples were considered for detailed investigation: Se/As_2S_3, GeSe/GeS and Sb/As_2S_3. After electron-beam irradiation, i.e. pattern writing, the irradiated area was first observed under an Olympus BH-2 optical microscope at ×100 magnification. The observed picture was recorded with a digital camera.

Photobleaching was expected according to the literature [132] and our data on photo- and thermally induced processes. The written pattern was observable in all samples. In figure 4.38. we present the recorded pattern visualized under optical microscope in transmission mode. According to the dependence of the refractive index on the exposure which has already been determined (see fig. 4.26.), the optical microscopic observation in transmittance mode gives higher pattern contrast at bigger refractive index change. Hence, in the case of Sb/As_2S_3 the observable pattern contrast is the highest while in the case of GeSe/GeS sample the contrast is small.

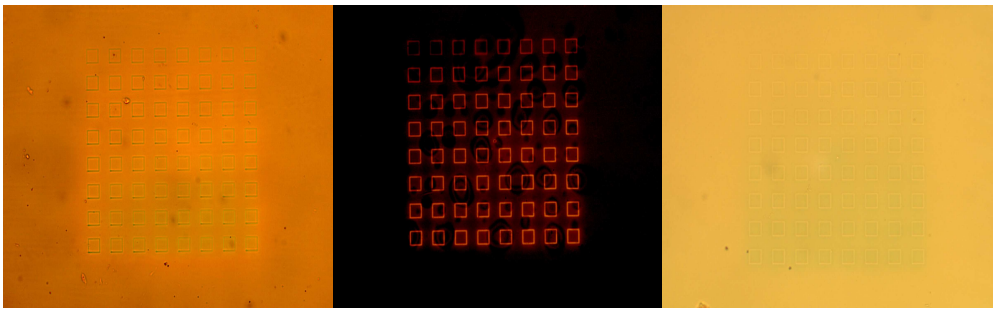

a) b) c)

Figue 4.38. Electron-beam patterning imprints under optical microscope of a) Se/As_2S_3, b) Sb/As_2S_3 and c) GeSe/GeS samples

Optical transmission change occurred as well in amorphous As_2S_3, where the magnitude was dependent on the time of irradiation and electron-beam density. In this case the determination of the *in situ* optical transmission change after or during electron-beam irradiation was not possible due to the small size of the area irradiated by e-beam.

AFM scanning was preformed in tapping mode almost immediately after irradiation, although the relief does not relax within months.

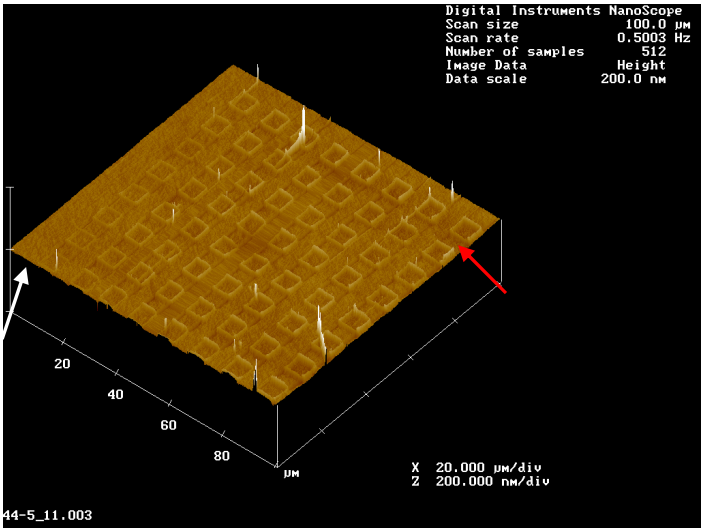

Figure 4.39. AFM surface scan after electron-beam lithography on Se/As_2S_3 nanolayered sample

The dose of irradiation was increasing from square to square during the electron-beam patterning. The lowest dose corresponding to the square in the left corner (white arrow in fig. 4.39.) was set to 0.1 C/cm^2, while the highest dose corresponding to square in the right corner (red arrow in fig. 4.39.) was set to 3 C/cm^2. The same procedure was applied for Sb/As_2S_3 and GeSe/GeS samples, as well. Investigations show that volume change appeared only in the cases of Se/As_2S_3 and GeSe/GeS samples. Sb/As_2S_3 does not show volume change after electron-beam irradiation. Nevertheless, the change of the refractive index is noticeable, as presented in figure 4.38 (b), and it is comparable to the results of optical measurement.

The electron-beam patterned samples were subjected to detailed AFM investigation. As Sb/As_2S_3 samples did not show any volume change after patterning, the investigations of the surface were focused on Se/As_2S_3 and GeSe/GeS samples. These more detailed AFM investigations of the electron-beam irradiated area were aimed to reveal the conditions which are suitable for maximum volume change and one-step electron lithography method. For this purpose numerous experiments have been done with different area dose matrix patterning. Irradiated areas were investigated

in a one-by-one manner, as presented in figure 4.40. for the Se/As_2S_3 sample and in figure 4.41. for the GeSe/GeS one.

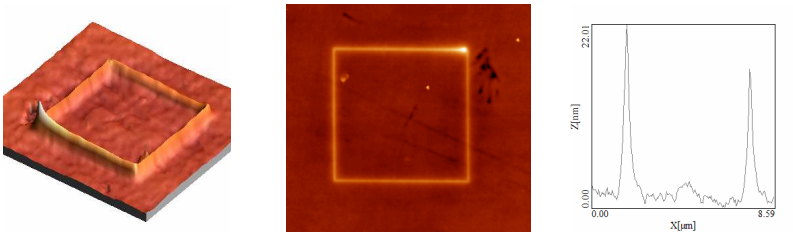

a) b) c)

Figure 4.40. AFM surface analysis of the irradiated Se/As_2S_3 surface, a) 3d surface scan, b) 2d surface scan, c) cross section

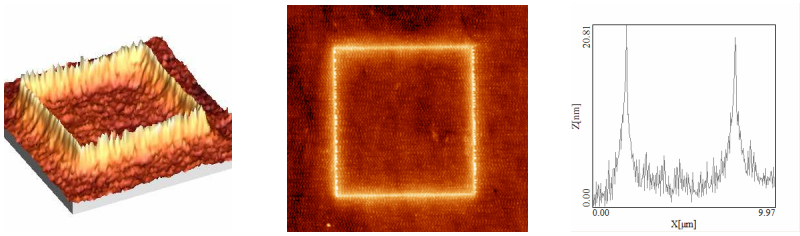

a) b) c)

Figure 4.41. AFM surface analysis of irradiated GeSe/GeS surface, a) 3d surface scan, b) 2d surface scan, c) cross section

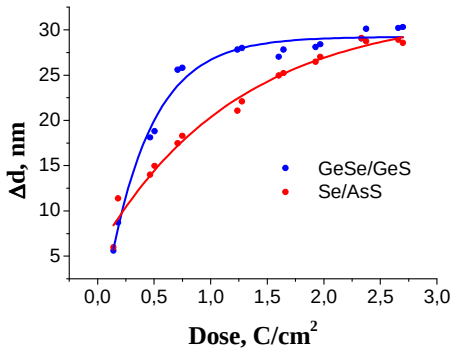

Figue 4.42. Relative volume (thickness) change of the layer after electron-beam irradiation

As it was observed and described in Chapter 4, the main difference between Se/As_2S_3 and GeSe/GeS samples after laser light illumination was the surface roughness, which originated from the different preparation methods. This effect is confirmed here, as well. The sample prepared by PLD technique differs mainly in the surface roughness. The relative volume change (see figure 4.42.) vs. irradiation dose above 2.5 C/cm^2 is the same for both types of nanolayered samples.

The expansion, measured in nanolayered samples and in the separate components (Se and As_2S_3) under similar conditions reveals that effects in sub-layers are not additive. The sum of expansions in separate layers is about only 30% of the total expansion measured in nanolayered samples. It means that e-beam intermixing enhances the extension process, but on the whole it takes place in combined materials, as well as–in the resulting As-S-Se mixture. AFM cross-sections of induced volume change are presented on figure 4.43.

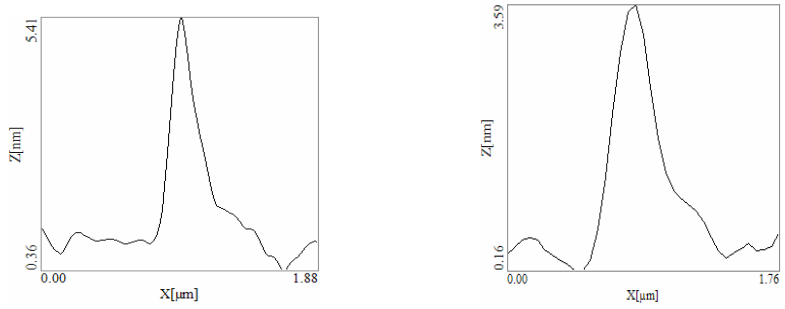

(a) (b)

Figure 4.43. Volume expansion of separate thin layers of Se (a) and As_2S_3 (b).

In the next step we irradiated the whole area of a single square. Appropriate dose recalculations were applied for the given area and the same idea and configuration were used as a preliminary in the case of the patterned shapes of single squares. The result of AFM surface observation is shown in figure 4.44.

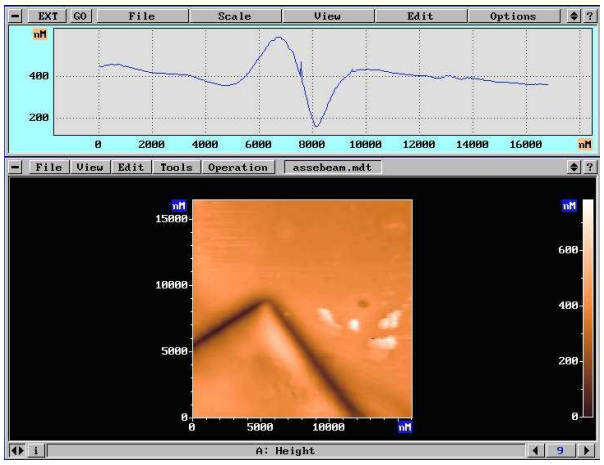

Figure 4.44. Full area irradiation of Se/As_2S_3

As it is well seen, the essential volume change appears mostly at the borders of the irradiated area. The situation, however, is more complex. Patterning a matrix of 8 × 8 full squares onto the Se/As_2S_3 nanolayered sample reveals that homogenous bleaching is observable in the irradiated areas in transmission under optical microscope.

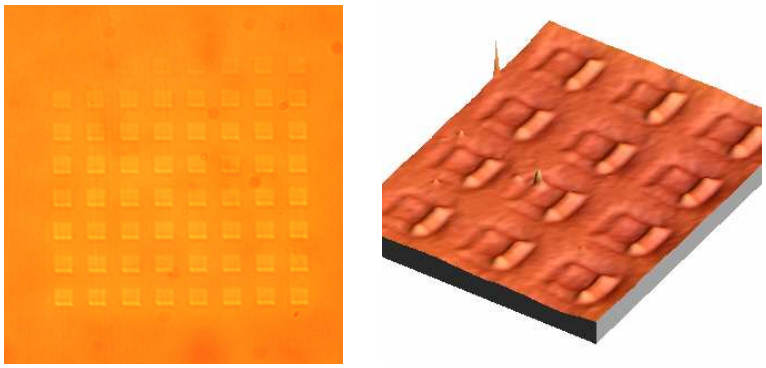

(a) (b)

Figure 4.45. Full area irradiation matrix with different doses: (a) optical microscope; (b) AFM of a segment

The magnitude of the bleaching corresponds to the irradiated dose, i.e. the lowest dose appears at the upper left corner and the highest dose at the lower right corner (see figure 4.45.(a)). AFM observation of the same area yields similar results to the observation from the preliminary experiment presented in figure 4.43. The AFM surface scan of a

segment is presented in figure 4.45.(b). It is noticeable that volume expansion occurred mostly at the border of the irradiated areas, where the scan ends and the e-beam returns back. An additional dose was possibly added here to the sample. In the case of a simple spot (or a lens-like cup) the picture is more definite (see.Fig.4.46)

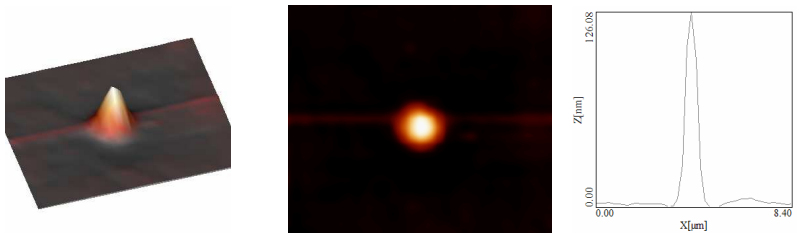

Figure 4.46. Spot irradiation of Se/As_2S_3

Thesis based on corresponding chapter

3. I have performed experiments to study the influence of electron irradiation on the characteristics of chalcogenide layers and nanolayered structures, with a special attention given to the changes of the structure and optical parameters. Comparison of the photon-induced optical and volume changes with the volume changes induced by electrons allows me to make the conclusion that they depend equally on the irradiation energy. I have established that the basic mechanism of the changes is similar.

5. Mechanism of induced changes

Photoinduced and electron-beam-induced processes have been assumed to activate similar structural changes in the investigated glasses, since both are able to excite the electronic system which can trigger atomic displacements. The response of the electronic system depends on energy distribution of localized states, which in turn is connected with composition, treatments and the fabrication technology.

Both the thermal treatment and optical irradiation affect the interdiffusion within a given sample. In the case of Se/As_2S_3 NLS the thermal and optical bias on the interdiffusion process appear just above room temperatures. In other chalcogenide-chalcogenide samples this range shifts to the higher temperatures, according to the Tg of components.

It was established that the thermal diffusion coefficients at 100°C are equal to:

$D(Se/As_2S_3) = (2.2 \pm 0.5) \times 10^{-22}$ m^2/s;

$D(GeSe/GeS) = (2.1 \pm 0.5) \times 10^{-22}$ m^2/s;

$D(Sb/As_2S_3) = (5 \pm 5) \times 10^{-23}$ m^2/s;

These data indicate that the diffusion process is probably more or less independent form the composition in chalcogenide-chalcogenide NLS, where the movement of chalcogen plays main role. The case of Sb-chalcogenide NML is exceptionally interesting, since the thermally induced diffusion is slow at room temperature, but it is essentially enhanced by illumination ($D_{photo} = 1{,}06 \times 10^{-21}$ m^2/s). This fact can be related to the peculiarities of diffusion and bond creation of Sb in the chalcogenide matrix, as well as to the known enhanced sensitivity of Sb to the light excitation used in the photomultipliers.

In spite of these differences the total (by light and e-beam) introduced energy which is necessary to achieve measurable structural changes and optical effects is approximately the same, so the diffusion processes in NMLs correlate in the whole and the mechanisms of structural changes due to the intermixing under illumination or e-beam can be assumed to be similar.

The diffusion of components in the gradient of their concentration either in a simple non-uniformly excited layer or in the nanolayered structure under existing conditions of photon-(electron) induced plasticity of the chalcogenide glass seems to be a basic effect in these materials [133, 134]. The process can be regarded as jumps of atoms or structural elements into the nearby micropores or microspaces. At high temperatures and comparatively low pressures, the quantity and the size of such microspaces in fluids or melts are high while, on the contrary, at low temperatures and high pressures they just begin to develop. The "free volume" theory assumes that the vacancies appear during reorganization of molecules or other structural elements, which is induced by thermal fluctuation (or incident of other phonon). In this way a free volume will be concentrated in a space close to a structural element which contains the defect. The lifetime of the defect will be not less than the lifetime of the excited electron-hole pairs (usually near $10^{-3} – 10^{-4}$ s in chalcogenides [44]), but it can be much higher for connected electron-hole pairs like valence-alternating pairs, etc [35]. This can be the reason of additive effects at continuous line recording by e-beam, which results in the formation of match-stick structures, as mentioned below.

E-beam recording of dots, lines or closed loops (rectangles) in Se/As_2S_3 NLS resulted in optical bleaching and local expansion, similarly to the laser beam. The expansion can be as high as 5-10 % of the initial thickness of the NLS, although in some samples it is even larger. As mentioned, the expansion of separate components (Se and As_2S_3) reveals that the effects in sub-layers are not additive. The sum of expansions in separate layers is about 30% of the expansion in NLS. It means that the e-beam intermixing enhances the extension process, but on the whole it takes place in combined sub-layers, as well as in the resulted As-S-Se mixture.

The observed non-linearity of the laser and the e-beam stimulated expansions over a certain power or current densities can be attributed to the heating effects. These heating effects influence not only the rate of charge and defect generation, but the change of the viscosity (and the thermal component of the diffusion coefficient) as well, in addition to the pure irradiation–stimulated one.

In this way the efficiency of mass transport, defect migration and structural changes increase exponentially which results in the measured dependences of volume

changes (presented in fig.4.42) [135]. If the defects and appropriate localized charge carriers belong to the different structural elements (chains and sheets) [117], the simple Coulomb interaction could also contribute to the volume change. This is possible only under limited conditions of decreased viscosity of the excited glass volume, enabling the extension towards the surface due to the internal pressure. If the e-beam irradiation induces viscosity change similar to the photo-stimulated one, a pre-softened area with decreased viscosity will move in front of the e-beam pulse. In this way the resulting expansion will increase at the same exposition. This can be the explanation of the match-stick shape of the recorded line or the spiral growth in the closed loop. In this case the radial distribution of viscosity change varies according to the electron scattering in the layer.

The pressure dependence of the photo-stimulated interdiffusion in NLS supports the important role of the defects and voids in interdiffusion and expansion processes [136]. Since the minimum energy necessary for the formation of an elemental free volume V_h (a hole analogous to a vacancy) is equal to the work made against the internal pressure: $E_h = HV_h$, where H is the microhardness [137], the photo-(electron beam) "softening" of the structure enhances the formation of additional free volume. This volume is frozen in after the cessation of the excitation. In this way "softening" gives possibly the main contribution to the observed expansion effects in a simple layer and in NML.

It should be noted, that the initial structure and composition, as well as the technology of the homogeneous or composite materials have a very important and sometimes unpredictable influence on the discussed expansion effects. This can also be one of the reasons of the discrepancies found in the published papers. In our case the presence of highly absorbing and fast diffusing metal in the Sb/As_2S_3 NLS caused large optical changes. At the same time it may cause fast dissipation of additional charges, which reduces the Coulomb repulsion part of the expansion. The increased rigidity can be a more important factor of the NLS and of the resulting mixture as well, since Sb_2S_3 structural elements and free As or arsenic oxides are formed in mixture regions according to the XPS measurements. It is worth mentioning that octahedral position of

As atoms in As_2O_3 or/and As_2S_3 could be substituted by Sb atoms without vacancy creation [138].

Some additional remarks follow from the presented e-beam recording results:

- the conservation of the volume seems to be not fulfilled. See the example in Figure 5.2, where no essential depression is detectable around the bump,

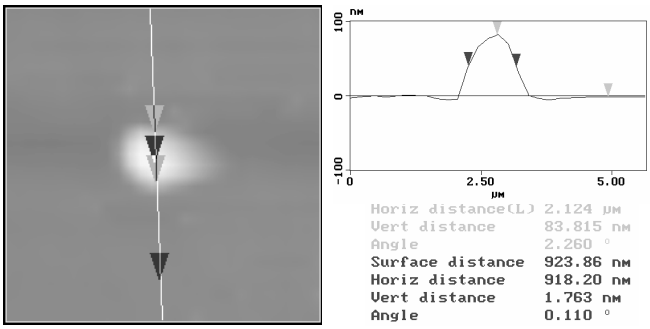

Figure 5.2. Electron-beam induced microlense

- the local expansion is increased along the line of the e-beam spot movement, making additional bumps at the corners and at the end of the line (the effect of the "match-stick", figure 5.3)

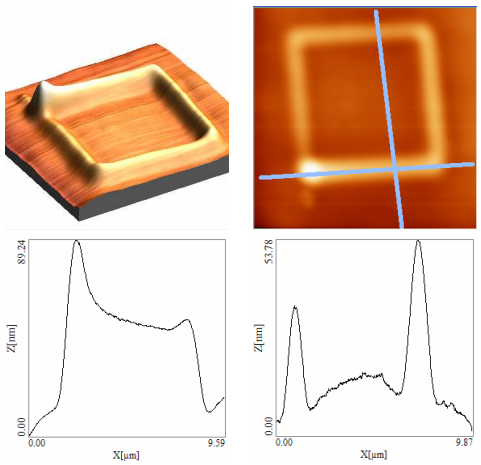

horizontal cross section vertical cross section

Figure 5.3. AFM scan of electron-beam induced square with appropriate cross sections

- the typical total input energy in the case of laser irradiation was 21.6×10^3 J/cm^2 and in the case of electron irradiation 4.8×10^3 J/cm^2 which reveals the importance of the direct energy conversion (possibly the number of generated charge carriers, i.e. simultaneously created defects and vacancies) for the realization of certain structural transformations (interdiffusion and expansion or just the creation of new multicomponent material).

Following the novel theoretical considerations on the lateral mass transport in the non-homogeneously irradiated chalcogenide layers the investigated e-beam induced surface relief formation mechanism can be further developed taking into account the surface tensions, defect generation rates (which are less predictable in the avalanche conditions of high energy electron impacts), heating effects, etc.

Thesis based on corresponding chapter

4. By X-ray diffraction measurements I have established the diffusion coefficients and compared the intermixing in different multilayers. The results show that the mechanism of the diffusion process does not depend essentially on the composition of the samples but rather on the peculiar defect structure of the amorphous chalcogenide material. This is supported by the time dependent changes of optical transmission at low temperatures, which are determined by the bonding defects, vacancies (micropores).

6. Applications of direct surface patterning

The change of electric conduction characteristic of Sb/As_2S_3 nanolayered samples was measured during illumination. The time dependence is shown in figure 6.1.

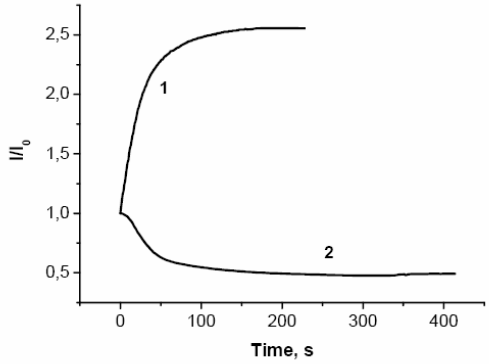

Figure 6.1. Photobleaching (1) and electric conduction kinetics (2) in Sb/As_2S_3 sample

According to such behaviors this kind of structure is applicable for the detection and measurement of light and electron-beam doses by measuring the lateral resistance of the parallel antimony layers in the NLS.

In addition to the number of known possibilities of optical data recording on chalcogenides, the developed Sb/As_2S_3 nanolayered structures could be applied for this purpose with higher efficiency because of higher refraction index and optical transmission change [139].

Diffraction gratings are also an opportunity for precise IR optical applications. The appropriate change of grating efficiency of these samples was observed by the measurement of the kinetics of the first reflected diffraction peak, when the grating was written by the projected interference pattern of two coherent green laser beams. The obtained results are presented in Fig. 6.2 for different samples.

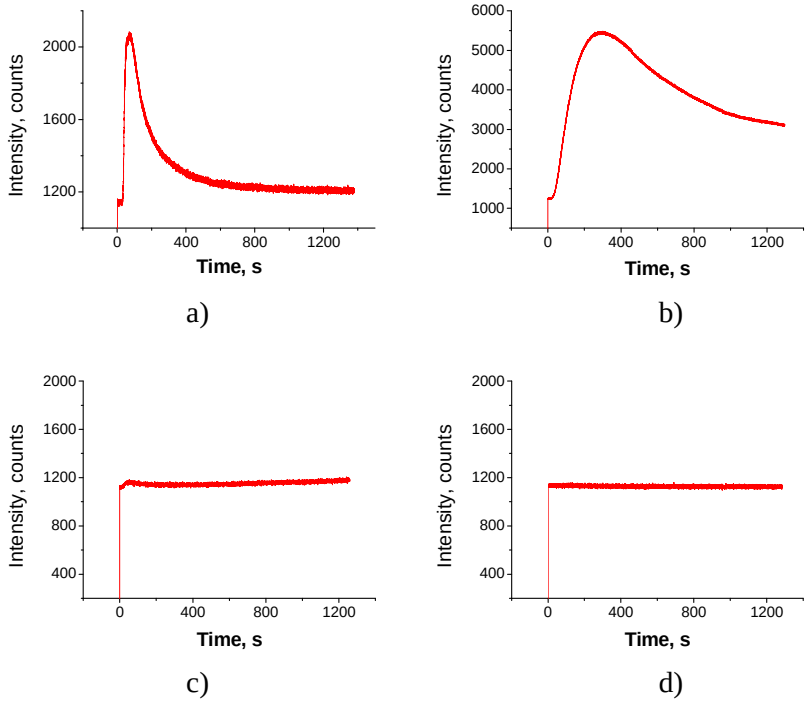

Figure 6.2. The kinetics of intensity change in the first diffraction peak for a) As_2S_3, b) Se/As_2S_3, c) Sb/As_2S_3, d) In/As_2S_3

In the case when nanolayered structure contains metal constituents, no volume expansion was observed. This effect makes them suitable for performing pure amplitude-phase modulation diffraction grating without local expansions, which can introduce undesirable stresses and image deformations in the optical element.

Micro-nano devices can also be fabricated by direct, one-step electron-beam patterning, without undesirable wet- or dry etching, as is known in normal resists [140]. The artificially induced effect of match-head formation was avoided by patterning one object, as Fresnel lenses or others, in several steps.

As an example for patterned objects, optical element prototyping, electron-beam created micro scattering lens on Se/As_2S_3 is presented in figure 6.3.

Figure 6.3. AFM picture of scattering lens (radius r=10μm)

With a specially developed program for e-beam patterning system, presented in figure 3.7, it is possible to create Fresnel lenses with predefined parameters. One of such lens is presented in figure 6.4.

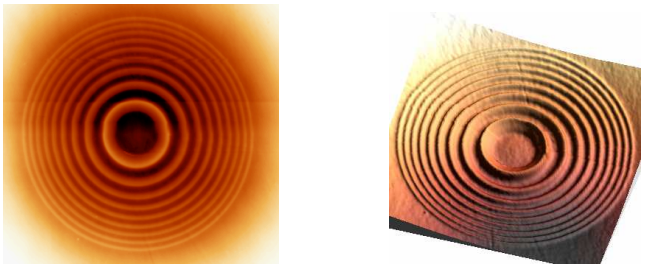

Figure 6.4. AFM picture of a Fresnel lens created on Se/As_2S_3 NLS (outer radius r = 10μm)

An advantage of such lenses is the small size, spectral sensitivity and possibility of tailoring spectral properties, based on the sample type. Of course, the e-beam prototyping of one or even more optical elements in a matrix needs some more time, in comparison with simple two-step resist, but the parameters of the element can be controlled immediately, *in situ*, and the multiplication process by imprint technology is possible either directly from the prototype to the plastic or via metal mold creation.

The idea of creating a micro-nano sized Green lens, which is presented in figure 6.5., is another possibility. For this purpose both types of nanolayered samples are suitable. In the case of Se/As_2S_3 the refraction index change will be accompanied by volume expansion, while in the case of Sb/As_2S_3 it is possible to create a refractive index gradient without volume expansion.

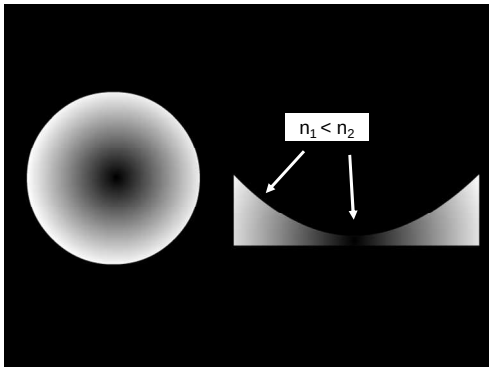

Figure 6.5. Fabrication of Green lenses

An array of needles is presented in figure 6.6. Their shape and geometry correspond to the described bump presented in figure 5.2.

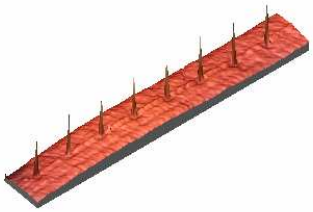

Figure 6.6. AFM picture of micro-comb with 5 μm periodicity

7. Summary and conclusions

Chalcogenide glasses or, more generally, amorphous chalcogenides are known as excellent materials for optoelectronics. The interest in amorphous nanolayered materials is caused by the wide range of tunable properties [9] by external excitation such as light, e-beam or other sources of energy [1], and by comparatively easy preparation and technological issues in comparison to other crystalline semiconductor materials. When the modulation period in layered structures falls in the range of few nanometers, new possibilities open for tailoring the properties of samples and for development of basic theories and applied solutions for photonics or electronics [4].

The most common technique for the production of amorphous thin layers is the TVE. In the case of nonstochiometric evaporation, PLD technique is can be considered. My experimental results show good agreement between the two sample preparation technologies [6, 103]. Thus, new sample formation is possible.

Investigation of laser light and e-beam induced volume expansion and surface pattern formation in the selected Se/As_2S_3, $Ge_{20}Se_{80}$/$Ge_{33}S_{67}$ and Sb/As_2S_3 nanolayered structures, as well as in simple Se and As_2S_3 layers as model ones, and in a number of similar structures revealed optical bleaching in all NLS [103, 104]. Volume expansion occurs only in chalcogenide-chalcogenide NLS and in the given homogeneous chalcogenide layers. Based on the comparison of these two different excitation and recording processes, the essential roles of pure electron-hole excitation, bond switching and thermal activation processes in the mechanisms of interdiffusion and relief formation are identified [105, 131].

First of all, the relief formation is connected with irradiation-induced electron-hole pair and defect creations, thus free volume increases during sample irradiation. The bond switching, and the possible additional influence of electrostatic forces, results in local mass transport [135].

Efficient photo- or thermally stimulated interdiffusion in Sb/As_2S_3 nano-multilayers is demonstrated and explained by interaction of antimony with sulphur atoms at the expense of As-S bonds [118]. The process is accompanied by the reaction of As-As units, and of antimony with oxygen at the surface. The exact role of oxygen in

the volume of multilayers is not clear yet. Explanation of the volume change in chalcogenides under illumination is mainly supposed to be connected with the presence of chalcogen-related “wrong bonds” and defects [118]. These defects are passivated by Sb atoms during interdiffusion in Sb/As_2S_3 NLS, while they continue to exist in Se/As_2S_3 NLS in which giant local expansion accompanies the photoinduced interdiffusion.

Large optical transmittance and refractive index change at relatively low light exposures without local change in volume are characteristic for interdiffusion in Sb/As_2S_3 NLS [140]. Therefore, these structures can be used as efficient media for optical amplitude-phase recording of patterns for optoelectronics [139].

Additional experiments on the influence of some metal and dielectric sub-layers on the stimulated expansion in nanolayered structures can be proposed and will help to verify the model. Efficient stimulated interdiffusion processes at low temperatures have been discovered and serve as a basis for further development of the models of light, e-beam stimulated diffusion processes in amorphous chalcogenides.

8. Összefoglalás

Bevezetés

A kalkogenidek kalkogén (kén, szelén, tellúr) és más elemek vegyülete, vagy ötvözete. Amorf Si és Ge mellett az amorf kalkogenidek, az elemi kalkogénekkel együtt, a szervetlen nemkristályos szilárd félvezető anyagok egyik legfontosabb csoportjába tartoznak [1, 2, 3]. Különleges tulajdonságuk, hogy külső sugárzás hatására (fény, hő, elektronok, ionok) akár többszörösen is képesek megváltoztatni a fizikai, kémiai tulajdonságaikat [1, 4], vagy - tipikusan csak az amorf kalkogenidekre jellemző módon - fotoindukált optikai elnyelési él-eltolódást [1] és indukált térfogatváltozást [2] mutatnak. Szerkezeti tulajdonságaik széles határok közt változhatnak, akár reverzibilis módon [9]. Mindez a nemegyensúlyi termodinamikai állapotának köszönhető. Az amorf kalkogenidek előállítása technológiailag lényegesen egyszerűbb a kristályos félvezetők előállításánál [5]. Ezért az amorf anyagok kutatása hosszú ideje a szilárdtestfizika és az anyagtudomány egyik legdinamikusabban fejlődő ága [3, 12].

Az utóbbi évtizedekben az optika, optoelektronika és a fotonika fejlődése következtében egyre nő az új optikai anyagok iránti igény. Különösen azon félvezető amorf anyagok kutatása indokolt, amelyek fizikai vagy elektromos tulajdonságai külső besugárzások hatására módosíthatók. Másrészt a szerkezeti változások és a diffúziós folyamatok vizsgálata nanoskálán mélyebb betekintést biztosít az anyagok viselkedésének feltárásában. Az amorf kalkogenidek tulajdonságai nanoskálán multirétegek előállításával vizsgálhatók [4, 5, 8].

A dolgozat célja saját eredményként ismertetett lézer- és elektron-besugárzás által amorf Se/As_2S_3, Sb/As_2S_3, $Ge_{20}Se_{80}$/$Ge_{33}S_{67}$ multirétegekben előidézett szerkezeti változások és domborzati mintázatok kialakulásának az összehasonlítása, a multirétegekben indukált keveredés mechanizmusának a mélyebb feltárása, valamint néhány gyakorlati alkalmazás megvalósításának a bemutatása.

Kísérleti eszközök és módszerek

Munkám során a következő kísérleti eszközöket és módszereket használtam. Multirétegeket kalkogenidek és más összetevők ciklikus vákuumgőzölése segítségével készítettem 99,999% tisztaságú anyagokból. Ennek a módszernek az a hátránya, hogy csak néhány ötvözetet lehet sztochiometrikusan gőzölni. Ezért lézerporlasztással és vákuumpárologtatással is készítettem ugyanolyan típusú mintákat. A minták tipikusan egymást követő 100 birétegből álltak, és az összvastagságuk nem haladta meg az 1 µm-t. Szerkezetüket Bruker gyártmányú IFS 55/FRA típusú Raman-spektroszkópiai berendezéssel vizsgáltam és hasonlítottam össze. Kisszögű röntgendiffrakció méréssel ellenőriztem a határfelületek minőségét. A határfelületek indukált keveredéséből pedig diffúziós állandókat határoztam meg. Shimadzu UV-3600 típusú optikai spektrofotométer segítségével végeztem az optikai áteresztőképesség mérését. Az áteresztőképesség időbeni változását lézerbesugárzás hatására pedig OceanOptics típusú spektrométerrel mértem, milliszekundumos időfelbontással. A kémiai állapot feltérképezése céljából röntgenspektroszkópiai méréseket Scienta ESCA-300 típusú berendezésen végeztem és a CasaXPS szoftverrel értékeltem ki a kapott spektrumokat. Elektronokkal LEO 1550 VP FE típusú pásztázó elektronmikroszkópban végeztem besugárzást és az így besugárzott minták felületét Digital Instruments DI-3000 és Solver P7 típusú atomerő-mikroszkópokkal vizsgáltam.

Eredmények és következtetések

Raman-spektroszkópiai kísérletekkel megállapítottam, hogy vákuumpárologtatással és lézerporlasztással előállított Se/As_2S_3 minták azonos szerkezeti tulajdonságokkal bírnak [6, 103]. Ezeket a méréseket fotospektroszkópiai mérésekkel kiegészítve, ugyanolyan optikai tulajdonságokat tapasztaltam a kétfajta mintakészítési eljárás által készített mintákon. Nevezetesen, az optikai áteresztőképességük ugyanolyan mértékben változott [103], az elnyelési él mindkét esetben a rövidebb hullámhossz tartomány felé tolódott el, továbbá a lézerbesugárzás által indukált térfogatváltozás mértéke megegyezett [103]. Lényeges eltérés a minták

morfológiájában és felületi durvaságban volt [103]. Vákuumpárologtatással simább felületű mintákat tudtam előállítani. Következésképpen új összetételű multiréteg kalkogenidek előállítására mindkét minta-előállítási módszer alkalmazható. Ezáltal lehetőség nyílik új, az irodalomban eddig nem ismert multirétegek előállítására. Így, munkám során pl. $Ge_{20}Se_{80}/Ge_{33}S_{67}$ multiréteget vizsgáltam és hasonlítottam össze az irodalomban már jól ismert multirétegek tulajdonságaival [104]. A kísérletek azt mutatják, hogy a $Ge_{20}Se_{80}/Ge_{33}S_{67}$ multiréteg ugyanolyan mértékű térfogatváltozást mutat, mint a Se/As_2S_3 multiréteg, de az optikai érzékenységi tartománya sokkal szűkebb [104], ami kedvező lehet gyakorlati alkalmazásoknál.

Fémet vagy félfémet (Bi, Sb, In, Au) tartalmazó multirétegek elektronokkal vagy fotonokkal való besugárzásra nem mutattak indukált térfogatváltozást, mint a jól ismert kalkogenid anyagok ($As_{20}Se_{80}$, As_2S_3), vagy az ezekből előállított amorf multirétegek [105]. Viszont az optikai tulajdonságokban bekövetkezett változások ugyanolyan jelleget mutatnak: az áteresztőképességük növekszik, törésmutatójuk változik. A kisszögű röntgendiffrakciós mérések pedig azt mutatják, hogy az egymást követő rétegek összekeverednek [118].

Szisztematikus méréseket végeztem fénnyel és elektronokkal való besugárzás összehasonlítására a fent említett mintákon és összetevőiken. Ezeket elektronlitográfiai módszerrel és milliszekundum felbontású optikai spektrométerrel mért optikai áteresztőképesség változás mérésével hajtottam végre. Atomerő-mikroszkópos mérések azt mutatják, hogy a Se/As_2S_3 és a $Ge_{20}Se_{80}/Ge_{33}S_{67}$ mintákban elektron-besugárzással indukált térfogatváltozás a besugárzási energia függvényében ugyanolyan mértékben változott [131], hasonlóan a lézerbesugárzáshoz. Ugyanez érvényes a törésmutató változásra és az optikai áteresztőképesség változásra is [140]. Ez egyértelműen a két rétegstruktúrában lejátszódó változás alapvető mechanizmusának a hasonlóságára utal. Kiegészítve az indukált diffúziós együtthatóknak az összehasonlításával arra a következtetésre jutottam, hogy a diffúziós folyamat mechanizmusa nem függ számottevően a minták összetételétől [118].

A röntgenspektroszkópiai mérések pedig magyarázatot adnak az indukált folyamat mechanizmusára. Amíg a különböző összetételű kalkogenid-kalkogenid, kalkogenid-kalkogén rétegszerkezetek indukált térfogatváltozásra hajlamosak, addig a

fémet vagy félfémet tartalmazó minták nem. Ezt a kémiai kötések megbomlása és új kötések kialakulása indokolja [118]. Az alacsonyhőmérsékletű optikai áteresztőképesség időbeni változása a keveredési folyamat részletéről ad kiegészítő információt. Alátámasztja a rácshiba képződést, a vakancia (mikropórus) és a kötéshibák által előidézett nanorétegek keveredését, és magyarázatot ad a multirétegek által nyújtott nagyobb mértékű térfogati változásokra is [140].

Az amorf nanorétegelt kalkogenidek különleges tulajdonságainak köszönhetően széleskörűen használhatók, mint könnyen formálható fotonikai-, optikai eszközök [139].

Definition of acronyms used

NML – nanomultilayers

ChG – chalcogenide glass

NLS – nanolayered structure

PLD – pulsed laser deposition

TVE – thermal vacuum evaporation

SRO – short range order

MRO – medium range order

LRO – long range order

AERDF – atomic-electronic radial distribution

CRN – continuous random network

RNM – random network model

CCM – constraint counting model

CFO – Cohen-Fritzsche-Ovshinsky model

DM – Davis-Mott model

CBD – charged dandling bonds

VAP – valence-alteration pairs

IVAP – intimate valence-alternation pairs

XPS – X-ray photoelectron spectroscopy

LAXRD – low angle X-ray diffraction

AFM – atomic force microscope

SEM – scanning electron microscope

RMS – root mean square

FWHM – full width at half maximum

Acknowledgements

I would like to thank:

Prof. Kökényesi Sándor, who was my supervisor at University of Debrecen, Department of Experimental Physics and introduced me into the world of science, and his enthusiasm for scientific research.

Dr. Himanshu Jain from Lehigh University who accepted me in his International Materials Institute for New Functionality in Glass research group.

Dr. Andrij Kovalsky, Dr. Alan Miller from Lehigh University at Department of Material Science and Engineering. I really appreciate they numerous discussion we had together about XPS technique and evaluation of results.

Dr. Floyd Miller from Lehigh University at Experimental Physics Department, who involved me into the electron-beam lithography technique.

Dr. Csík Attila from Institute of Nuclear Research of the Hungarian Academy of Sciences, who have helped me with low angle X-ray diffraction measurements.

Dr. Petr Nemec from University of Pardubice for his accomplishment with PLD sample preparation technique and Raman-spectroscopy.

Institute of Nuclear Research of the Hungarian Academy of Sciences for support me in my scientific research from 2009 to 2012.

Finally a special thanks to Dr. Vad Kálmán and Dr. Hakl József for endless and very precious moral and logistical support during the last couple of years.

References

[1] А. Фельц “Аморфные и стеклообразные неорганические твердые тела”, Пер. с нем. – Москва, Мир (1986)

[2] Борисова З.У. “Халькогенидные полупроводниковые стекла”, изд-во Ленингр. ун-та (1983)

[3] А. В. Стронський, М. Влчек, А. Скленарж, П. Ф. Романенко, С. А. Костюкевич “Оптоэлектроника и полупроводниковая техника” **34**, 65 (1999)

[4] A.V.Kolobov “Photo-Induced Metastability in Amorphous Semiconductors”, Whiley, Weinheim (2003)

[5] A.Goswami “Thin Film Fundamentals”, New Age International (1996)

[6] P.Nemec, V.Takats, A.Csik, S.Kokenyesi, J. Non-Cryst. Solids **354,** 5421 (2008)

[7] Alvin W. Czanderna at.al. ”Specimen Handling, Preparation, and Treatments in Surface Characterization”, Kluwer Academic Publisher (2002)

[8] G.Timp “Nanotechnology”, Springer – Verlag New York (1999)

[9] Г.З.Виноградова “Стеклообразование и фазовые равновесия в халькогенидных системах. Двойные и тройные системы.”, Москва, Наука (1984)

[10] Vateva, in Phys. and Appl. of Non-Cryst. Semicond. in Optoel., A. Andriesh and M. Bertolotti (eds.), Kluwer Academic Publishers, Dodrecht-Boston- London (1997)

[11] S.Kökenyesi, J. Optoelectronics and Adv. Materials **8**, 2093 (2006)

[12] A.Madan and M.P.Shaw, “The Physics and Application of Amorphous Semiconductors”, Academic Press, Inc., San Diego, 1988

[13] C.Kittel “Bevezetés a szilárdtest-fizikába”, Műszaki Könyvkiadó (1981)

[14] S.R.Elliott, J. Non-Crystalline Solids **81**, 71-98 (1986)

[15] M.L.Trunov at.al., Appl.Phys.Lett. **97**, 031905 (2010)

[16] L. Pauling “The nature of the chemical bond”, Cornell University Press, Ithaca, New York (1960)

[17] P.W.Anderson, Phys.Rev. B **109**, 1492 (1958)

[18] N.F.Mott, Adv.Phys. **16**, 49 (1967)

[19] D.E.Polk, J. Non-Cryst. Solids **5**, 365 (1971)

[20] Steinhardt, R.Alben, M.S.Duffy and M.S.Polk, Phys. Rev. B **18**, 6021 (1973)

[21] M.Popescu, Ph. D. Thesis, Bucharest, 1975

[22] P.Visor, J. Non-Cryst. Solids **101**, 156 (1988)

[23] M.Popescu, J. Non-Cryst. Solids **192&193**, 140 (1995)

[24] М.Бродски „Аморфные полупроводники", Москва, Мир (1982)

[25] R.M.White, J. Non-Cryst.Solids **16**, 387 (1974)

[26] J.C.Philps, J.Non-Cryst.Solids **34**, 153 (1979)

[27] J.C.Philips, J.Non-Cryst.Solids **43**, 37 (1983)

[28] J.C.Philips, J.Non-Cryst.Solids **35-36**, 1157 (1980)

[29] J.C.Phillips and M.F.Thrope, Solid State Commun. **53**, 699 (1985)

[30] M.F.Thrope and J.C.Phillips, J.Non-Cryst.Solids **57**, 355 (1983)

[31] W.A.Kamitakara, R.L.Cappelletti, P.Boolchand, B.Halfpap, F.Gompt, D.A.Neumann and K.Mukta, Phys.Rev.B **44**, 94 (1991)

[32] M.Tatsumisago, B.L.Halfpap, J.L.Green, S.M.Lindsay and C.A.Angell, Phys.Rev.Lett. **64**, 1549 (1990)

[33] K.Tanaka, J.Non-Cryst.Solids **103**, 149 (1988)

[34] M.H.Cohen, H.Fritzsche, S.R.Ovshinsky, Phys.Rev.Lett. **22**, 1065 (1969)

[35] E.A.Davis and N.F.Mott, Philos.Mag. **22**, 903 (1970)

[36] P.W.Anderson, Phys.Rev.Lett. **34**, 953(1975)

[37] N.F.Mott, E.A.Davis and R.A.Street, Phil.Mag. **34**, 961 (1975)

[38] M.Kastner, A.Adler and H.Fritzsche, Phys.Rev.Lett. **37**, 1504 (1976)

[39] M.Kastner and H.Fritzsche, Phill.Mag.B **37**, 199 (1978)

[40] J.Robertson, Phys.Chem.Glasses. **23**, 1 (1982)

[41] M.Kastner, Phys.Rev.Lett. **28**, 355 (1972)

[42] S.R.Ovshinsky, Phys.Rev.Lett. **36**, 1469 (1976)

[43] M.Kastner, A.Adler and H.Fritzsche, Phys.Rev.Lett. **37**, 1504 (1976)

[44] Н.Мотт, Э.Девис, "Елекронные процессы в некристаллических веществах", Пер. с англ. – Москва, Мир (1974)

[45] А.А.Айвазов, Б.Г.Будагян, С.П.Вихров, А.И.Попов „Неупорядочненные полупроодники" – Москва, Высшая школа (1995)

[46] D.Strand, J. Optoelectronics and Adv. Materials **7**, 1679 (2005)

[47] R.Zallen. *The Physics of Amorphous Solids* (John Wiley &Sons, N.Y., 1983)

[48] S.R.Elliott, "Materials Science and Technology", VCH, Weinheim, **9**, 375 (1991)

[49] T.P.Russell et al. Nature, **365**, 235 (1993)

[50] T.Ohta, N.Akahira, S.Ohara, I.Satoh. Optoelectronics, **10**, 361 (1995)

[51] K.Tanaka, J.Non-Cryst.Solids **35&36**, 1023 (1980)

[52] K.Tanaka, Phys.Rev.B **57**, 5163 (1998)

[53] Д.К.Таганцев, С.В.Немилов, Физ. И хим. Стекла **15**б, 397 (1989)

[54] H.Hisakuni, K.Tanaka, Science **270**, 974 (1995)

[55] V.Kolobov, S.R.Elliott, Adv.Phys. **40**, 625 (1991)

[56] K.Shimakawa, A.Kolobov, S.R.Elliott, Adv.Phys. **44**, 475 (1995)

[57] В.М.Любин, Фотографические процессы на основе халькогенидных стеклообразных полупроводниов, в Несеребрянные фотографические процессы. под ред. А.Л.Картужанского. –Ленинград: Химия, 1984.

[58] S.R.Elliott, J.Non-Cryst.Solids **81**, 71 (1986)

[59] G.Pfeiffer, M.A.Paesler, S.C.Agarwal, J.Non-Cryst Solids **130**, 111 (1991)

[60] K.Shimakawa, A.Kolobov, S.R.Elliott, Adv.Phys. **44**, 475 (1995)

[61] V. K. Malinovsky, A. P. Sokolov, Sol. State Commun **57**, 757 (1986)

[62] Malyovanik M., Kökényesi S., Messaddeq S.H., Messaddeq Y., Iván I., Ribeiro S., J. Non-Crystalline Solids **348**, 144 (2004)

[63] А.О.Матковский, Д.Ю.Сугак, С.Б.Убизский „Воздействие ионизирующих излучений на материалы электронной техники", Львов, Світ (1994)

[64] Под ред. Б.И.Болтакса, Т.В.Машовец, А.П.Орлова „Точечные дефекты в твердых телах", Москва, Мир (1979)

[65] K.Tanaka, Appl.Phys.Lett. **70**, 2 (1997)

[66] В.С.Макаревич, В.Г.Ремесник, В.Г.Цукерман „Электронно-лучевая запись информации в халькогенидных пленках", Л: Центр научно-технической информации "Поиск" (1979)

[67] J.C.Phillips, Topological model for no-radiative carrier decay in chalcogenide alloys glasses, Non-Cryst.Solids **41**, 179 (1980)

[68] Н.В.Гусак, Л.И.Литинская „Электронно-стимулированные изменения оптических констант в тонких пленках халькогенидных стекол”, Автометрия **5**, 26-28 (1988)

[69] M.T.Kostyshin, E.V.Mikhailovskaya, P.F.Romanenko, Soviet Phys.Solid. **8**, 451 (1966)

[70] M.Malyovanik, I.Ivan, A.Kikineshi, I.Mojzes, M.Shiplyak, I.Szabo, J.Torok, J.Opto. and Adv.Mat. **5**, 1199 (2003)

[71] V.Lubin, M.Klebanov, N.Froumin, Physica B **348**, 121 (2004)

[72] K.Tanaka, Y.Ichimura, M.Komaski, Thin Solid Film **19**, 51 (1990)

[73] H.Jain, J.Opto. and Adv.Mat. **5**, 5 (2003)

[74] M.T.Kostyshin, E.V.Mikhailovskaja, P.F.Romanenko, Soviet Phys.Solid.St. **8**, 451 (1966)

[75] A.V.Kolobov, S.R.Elliott, Adv. Phys. **44**, 475 (1995)

[76] I.Y.Indutnyi, V.A.Danko, A.A.Kudryavtsev, E.V.Michailovskaja, V.I.Minko, J. Non-Cryst. Solids **185**, 176 (1995)

[77] M.Malyovannik, I.Ivan, A.Kikineshi, I.Mojzes, M.Shipljak, I.Szabo, J.Torok, J. Opto. and Adv. Mat. **5**, 1199 (2003)

[78] K.V.Adarsh, K.S.Sangunni, S.Kokenyesi, I.Ivan, M.Shipljak, Phys. Chem. Glasses: Eur. J. Glass Sci. Technol. A **47**, 198 (2006)

[79] I.Ivan, G.Erdélyi, S.Kokenyesi, D.L.Beke, J. Non-Cryst. Solids **352**, 1591 (2006)

[80] J. Viens, C. Meneghini, A. Villeneuve, T. V. Galstian, É. Knystautas, M. A. Dugay, K. A. Richardson, T. Cardinal, J. Lightwave Technol. **17**, 1184 (1999)

[81] C.Lopez, K.A.Richardson, M. de Castro, S.Seal,D.K.Verma, A.Shulte, C.Rivero, A.Villeneuve, T.V.Gastian, K.Turcotte, A.Saliminia, J.Laniel, J. of the American Cramic Soc. **85**, 1372 (2002)

[82] Jianrong Qiu, Kiyotaka Miura, Kazuyuki Hirao, J. Non-Cryst. Solids, **354**, 1100 (2008)

[83] Junji Tominaga, Nanophotonics with Surface Plasmons, 171 (2007)

[84] Takeo Ohta, Masahiro Birukawa, Noboru Yamada, Kazuyuki Hirao, Journal of Magnetism and Magnetic Materials **242**, 108 (2002)

[85] S.R.Ovshinsky, J. Non-Cryst. Solids, **73,** 395 (1985)

[86] J.Mort, Physics Today **47**, 32 (1994)

[87] J.Rowlands and S.Kasap, Physics Today **50**, 24 (1997)

[88] M.Frumar, B.Frumarova, P.Nemec, T.Wagner, J.Jedelsky, M.Hrdlicka, J. Non-Cryst. Solids **352**, 544 (2006)

[89] R.Swanepoel, "Determination of the thickness and optical constants of amorphous silicon", J.Phys. E: Sci. Instrum. **16**, 1214 (1983)

[90] J.Tauc "Optical Properties of Solids", North-Holland, Amsterdam, 1970

[91] R.Swanepoel, J.Phys. E: Sci. Instrum. **16**, 1214-1222 (1983)

[92] R.Swanepoel, J.Phys. E: Sci Instrum. **17**, 896-903 (1984)

[93] E.Fullerton, I.K.Shuller, H.Vanderstraeten, Y.Bruynseraede, Phys.Rev. B **45,** 9292 (1992)

[94] V.L.Averianov, A.V.Kolobov, B.T.Kolomiets, V.M.Lyubin, Phys.Sat.Sol., **a 57**, 81 (1980)

[95] K.Tanaka, A.Odajima, Solid State Commun., **43**, 962 (1982)

[96] M.Frumar, B.Frumarova, T.Wagner, P.Nemec in *Photoinduced Metastability in Amorphous Semiconductors*, ed. by A.V.Kolobov (Whiley, Weinheim, 2003)

[97] P.Chen, P.Boolchand, D.G.Georgiev, *J. Phys.: Condens. Matter* **22**, 065104 (2010)

[98] В.П.Захаров „Связь оптических свойств со структурой напыленных халькогенидов мышьяка и сурьмы", Изв. АН СССР.Сер.неорган.материалы, Т.11, №3, 544-545 (1975)

[99] J.W.M.DuMound and J.P.Youtz, *J. Appl. Phys.* **11**, 357 (1940)

[100] M.L.Trunov, P.M.Nagy, V.Takats, P.M.Lytvyn, S.Kokenyesi, E.Kalman, J. Non-Cryst Solids **355**, 1993 (2009)

[101] S.Kokenyesi, I.Iván, V.Takáts, J.Pálinkás, S.Biri, I.A.Szabo, J. Non-Cryst. Solids **353**, 1470 (2007)

[102] S.Kökényesi, V.Palyok, I.Szabó, M.Shiplyak, I.Iván, D.Beke, J. Non-Cryst. Solids **326**, 484 (2003)

[103] V.Takats, P.Nemec, A.Csik, S.Kokenyesi, J.Phys.Chem.Sol. **68**, 948-952 (2007)

[104] P.Nemec, V.Takats, A.Csik, S.Kokenyesi, Journal of Non. Cryst. Sol. **354**, 5421-5424 (2008)

[105] V.Takats, P.Nemec, A.C.Miller, H.Jain, S.Kokenyesi, Optical Materials **32**, 667-679 (2010)

[106] S.Kokenyesi, D.Beke, K.S.Sangunni, V.Takats at.al., J. Mater. Sci. **20**, 107 (2009)

[107] I.Iván, S.Kökényesi, Journal of Optoelectronics and Advanced Materials **4**, 743 (2002)

[108] V.Takats, 17th International Symposium on Non-Oxide and New Optical Glasses, Ningbe 13-18 June (2010)

[109] R.Naik, K.V.Adarsh, R.Ganesan, K.S.Sangunni, S.Kokenyesi, U.Deshpande, T.Shripathi, J. Non-Cryst. Solids **355**, 183 (2009)

[110] R.I.Hegde, S.R.Sainkar, S.Badrinarayanan, A.P.B.Sinha, *J. Electron Spectrosc. Relat. Phenom.* **24**, 19 (1981)

[111] R.Izquierdo, E.Sacher, A.Yelon, *Appl. Surf. Sci*. **40**, 175 (1989)

[112] M.Hanafi, F.M.Ismail, *Zeitschrift fur Physikalische Chemie,* **268**, 593-7 (1987)

[113] L.Pauling *The Nature of the Chemical Bond* 3rd edn, New Delhi: Oxford and IBH (1967)

[114] A.Kovalskiy, H.Jain, A.Miller, R.Golovchak, O.Shpotyuk , *J. Phys. Chem. B* **110**, 22930 (2006)

[115] A.Gheorghiu, I.Lampre, S.Dupont, C.Senemaud, M.A.El Idrissi Raghni, P.E.Lippens, J.Olivier-Fourcade, J. Alloys and Compounds, v 228, n 2, 143-7 (1995)

[116] J.Singh, K.Shimakawa, Advances in Amorphous Semiconductors, CRC Press (2003)

[117] G.Chen, H.Jain, M.Vlcek, A.Ganjoo, *Phys.Rev.B* **74,** 174203 (2006)

[118] V.Takats, A.C.Miller, H.Jain, A.Kovalskiy, S.Kokenyesi, Thin Solid Film **519**, 3437 (2011)

[119] O.Shpotyuk, J.Filipecki "Free volume in vitreous chalcogenide semiconductors", Ed. Univ.Czestochowa (2003)

[120] G.Chen, H.Jain, M.Vlcek, S.Khalid, J.Li, D.A.Drabold, S.Elliott, *Appl.Phys.Lett*., **82,** 706 (2009)

[121] M.Malyovanik, S.Kökényesi, at.al. Journal of Applied Physics, **93**, 139 (2003)

[122] V.Takats, 17th International Symposium on Non-Oxide and New Optical Glasses, ISNOG (2010)

[123] V.O.Balitska, O.I.Shpotyuk, J. Non-Cryst. Solids **277**, 723 (1998)

[124] K.Tanaka, Appl.Phys.Lett **70**, 2 (1997)

[125] G.B.Hoffman at al., J.Vac.Sci.Technol.B **26**, 6 (2008)

[126] O.C.Wells "Scanning Electron Microscopy", New York: McGraw-Hill (1974)

[127] H.E.Bishop, Br.J.Appl.Phys., **18**, 703 (1967)

[128] K.Tanaka, *Appl.Phys.Lett.* **70**, 2 (1997)

[129] D.Drouin et al., Scanning **29**, 92 (2007)

[130] V.Takats, H.Jain, Cs.Cherhati, I.A.Szabo, D.Beke, S.Kokenyesi, ISNOG2008, Montpellier, France, 2008.Apr. 20-25, p.

[131] V.Takats, F.Miller, H.Jain, Cs.Cserhati1 and S.Kokenyesi, Phys. Status Solidi **C 6**, No. S1, S83 (2009)

[132] Макаревич В.С., Ремесник В.Г., Цукерман В.Г. "Электронно-лучевая запись информации в халькогенидных пленках" Л: Центр научно-технической информации "Поиск" (1979)

[133] M.Trunov, J.Non-cryst. Solids **192**, 431 (1995)

[134] F.D. Fischer, G. Reisner, E. Werner, K. Tanaka, G. Cailletaud, T. Antretter, International J. of Plasticity, **16**, 723 (2000)

[135] Yu. Kaganovskii, M.L. Trunov, D.L. Beke, S. Kökényesi, *Materials Letters* **66**, 159 (2011)

[136] I.Ivan, G.Erdélyi, S.Kokenyesi, D.L.Beke *J. Non-Cryst. Solids* **235,** 1591 (2006)

[137] S.Sanditov, H.M.Bartenev , Physical properties of disordered structures, "Nauka", Novosibirsk (1982) (in Russian)

[138] G.F.Brewster, J.R.Hensler, J.L.Rood and R.A.Weidel, *Applied Optics,* **5**, 1891 (1966)

[139] Войнарович І.М., Токач В.О., Шипляк М.М., Кикинеші О.О., Патент 94329 Україна, "Реєструючий матеріал для запису оптичних рельєфів", МПК G 03G 5/00 (2011)

[140] V.Takáts, F.C.Miller, H.Jain, C.Cserháti, I.A.Szabó, D.Beke, S.Kökenyesi, J. Non-Cryst. Solids **355**, 1849 (2009)